Chemical Science

ROYAL SOCIETY OF CHEMISTRY

EDGE ARTICLE

View Article Online
View Journal | View Issue

Cite this: *Chem. Sci.*, 2024, **15**, 13389

All publication charges for this article have been paid for by the Royal Society of Chemistry

Construction of intermolecular σ-hole interactions in rare earth metallocene complexes using a 2,3,4,5-tetraiodopyrrolyl anion†

Francis Delano, IV, [a] Florian Benner, [a] Seoyun Jang, [a] Samuel M. Greer [b] and Selvan Demir *[a]

The generation of noncovalent intermolecular interactions represents a powerful method to control molecular vibrations and rotations. Combining these with the axial ligand field enforced by the metallocene ligand scaffold provides a dual-pronged approach in controlling the magnetic-relaxation pathways for dysprosium-based single-molecule magnets (SMMs). Here, we present the first implementation of 2,3,4,5-tetraiodopyrrole (TIPH) in its anionic form $[TIP]^-$ as a ligand in three isostructural rare-earth metal complexes $Cp^*_2RE(TIP)$ (**1-RE**, RE = Y, Gd, and Dy; Cp* = pentamethylcylopentadienyl), where the TIP ligand binds through the nitrogen and one iodine atom $\kappa^2(N,I)$ to the metal centre. The shallow potential energy surface of the intermolecular σ-hole interaction yields distortions of the interatomic distances at elevated temperatures which were investigated by variable-temperature SCXRD. **1-RE** constitute the first crystallographically characterized molecules containing TIP as a ligand for any metal ion, and **1-Dy** is the first SMM that employs the TIP ligand. The structural dependence on temperature allowed the mechanism of magnetic relaxation to be explored through *ab initio* calculations at different temperatures. The electronic influence of the coordinated iodine substituent was probed *via* magnetometry and cw-EPR spectroscopy on **1-Gd**. To further scrutinize the impact of the iodine substituents on the physical properties, a second set of new complexes $Cp^*_2RE(DMP)$ (**2-RE**, RE = Y, and Dy) where DMP = 2,5-dimethylpyrrolyl were synthesized. Here, the DMP ligand binds similarly to the TIP ligand and represents an all-hydrocarbon analogue to **1-RE**. **2-Dy** constitutes the first SMM bearing a DMP ligand.

Received 10th June 2024
Accepted 29th June 2024

DOI: 10.1039/d4sc03786c

rsc.li/chemical-science

Introduction

Anionic heterocyclic rings represent attractive ligands for the generation of rare earth (RE) metal complexes, as they are typically isoelectronic to the ubiquitous cyclopentadienyl ligand. RE complexes bearing five-membered heterocyclic rings are rarer relative to the all-hydrocarbon analogues. The isolated examples comprise borolyl,[1,2] silolyl,[3] germolyl,[3,4] plumbolyl,[5] phospholyl,[6–9] arsolyl[10] and bismolyl[11] anions. Thus, exploring the interactions of substituted five-membered heterocyclic ligands with the RE metals represents a fundamental frontier of research as the synthetic strategies for the generation of substituted heterocyclic rings are typically well-investigated.[12–14] Recently, other pentadentate organometallic ligands such as carborane ligands have also been employed to construct dysprosium single-molecule magnets.[15–17]

The generation of noncovalent inter- and intramolecular interactions represents a powerful tool for (supra)molecular chemistry and crystal engineering.[18] Halogen bonding originates from a net attractive interaction between a charge depleted region of a halogen atom and a nucleophilic region of a molecule or molecular fragment.[19] σ-holes, or areas of positive electrostatic potential along the extensions of covalently bonded halogen atoms, stem from the charge density anisotropy of the heavy halogens. Consequently, negative electrostatic potential accumulate on the equatorial regions of the atom.[20] This phenomenon is typically observed for the heavy halogen atoms due to the increased polarizability ascribed to the larger ionic radii. Intermolecular interactions of this class have garnered enormous attention in supramolecular chemistry and related fields.[21]

Our search for ligand scaffolds suitable for fostering halogen bonding stabilization interaction led to the attractive 2,3,4,5-tetraiodopyrrole ligand (TIPH), Fig. 1. Excitingly, its electrostatic potential map reveals a region of depleted electron density, a key observable of σ-holes.[19] Generally, the positive

[a]*Department of Chemistry, Michigan State University, 578 South Shaw Lane, East Lansing, Michigan, 48824, USA. E-mail: sdemir@chemistry.msu.edu*

[b]*Los Alamos National Laboratory (LANL), Los Alamos, New Mexico 87545, USA*

† Electronic supplementary information (ESI) available. CCDC 2350192–2350216. For ESI and crystallographic data in CIF or other electronic format see DOI: https://doi.org/10.1039/d4sc03786c

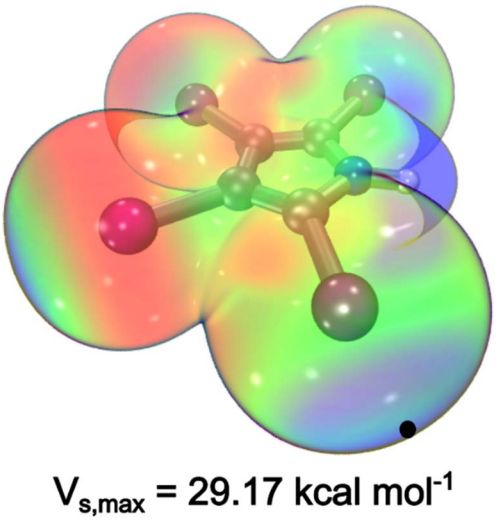

Fig. 1 Electrostatic potential of tetraiodopyrrole (TIPH) mapped on the contour of electron density. Calculations were completed at the TPSSh/def2-TZVP level, employing a 28-electron pseudopotential on I. The blue positive region located on the iodide substituents and the red negative region around the periphery is indicative of a σ-hole, corresponding to a $V_{s,max}$ of 29.17 kcal mol^{-1}.

extrema of the electrostatic potential, $V_{s,max}$, corresponds to the location of the σ-hole.[20] Notably, co-crystals containing TIPH and tetraphenylphosphonium iodide, tri(*n*-propyl)ammonium or 1,3,5-trimethylpyridinium iodide exhibit short I···TIP interatomic distances,[22,23] indicative of halogen bonding. Discrete installation of both halogen atoms and halogen-containing substituents has enabled a controlled design of catalysts and supramolecular structures. Remarkably, halogen bonding interactions were integral for the production of molecular motors and catalysts,[24] by helping maintain a specific geometry that best favours the rotational behaviour of said molecule.

We are intrigued to implement non-covalent interactions in the realm of the rare earth (RE) metals, using TIP, which is hitherto unexplored in coordination chemistry at large. In particular, our interest is to generate new single-molecule magnets (SMMs) featuring such non-covalent interactions and study their impact on the mechanism of magnetic relaxation.

Albeit its scarce use, TIPH is an intriguing molecule that was first discovered by Ciamician and Dennstedt in 1882.[25] The molecule itself is generally stable, however decomposes releasing I_2 at elevated temperatures (140–150 °C). As such, TIPH represents a promising material as an agent defeat weapon,[26] a molecule designed to destroy or neutralize active agents by releasing large amounts of biocides such as I_2 after detonation, owing to its inherent high iodine content, and impact sensitivity.

Herein, the synthesis and characterization of three unprecedented mononuclear yttrium, gadolinium, and dysprosium tetraiodopyrrole complexes $Cp^*_2RE(TIP)$ (**1-RE**, RE = Y, Gd, and Dy; Cp* = pentamethylcyclopentadienyl, TIP = 2,3,4,5-tetraiodopyrrolyl) are presented. The three isostructural complexes represent the first crystallographically characterized compounds containing TIP as a ligand for any metal ion. Noteworthy, the TIP ligand formally binds κ^2(N,I) to the metal centre involving both the nitrogen atom and the iodine atom of the 2-position of the heterocyclic ring. This binding motif was unambiguously confirmed through single-crystal X-ray diffraction (SCXRD) analysis and density functional theory calculations. As intermolecular halogen-bonding interactions may be prone to depend strongly on temperature,[27,28] the structure of **1-Dy** was thoroughly examined through variable temperature SCRXD. This strong intermolecular interaction manifests itself in a significant distortion to the primary crystal field of the Dy^{III} ion, as a result of the elongation of the intermolecular I···I interactions over the investigated temperature range. Excitingly, The Dy^{III} congener, **1-Dy**, displays out-of-phase components of the ac magnetic susceptibility, indicative of slow magnetic relaxation. The observed structural distortions with respect to temperature affords the opportunity to investigate how small alterations to the Dy–I distance influences the mechanism of magnetic relaxation through *ab initio* calculations at three different temperatures. Additionally, the electronic structure of **1-Gd** was probed through both magnetometry and cw-EPR spectroscopy, in order to assess the influence of the proximal iodine atom on the electronic structure of the Gd^{III} centre. The analogous 2,5-dimethylpyrrolyl complexes $Cp^*_2RE(DMP)$ (**2-RE**, RE = Y, Dy, DMP = 2,5-dimethylpyrrolyl) were additionally isolated. Here, the DMP ligand binds in a similar fashion to the tetraiodopyrrole ligand and represent excellent hydrocarbon analogues to the halogen substituted complexes.

Experimental methods

General information

All manipulations described below were performed under an inert N_2 or Ar atmosphere with rigorous exclusion of oxygen and moisture using Schlenk and glovebox techniques, unless otherwise noted. House nitrogen was purified through a MBraun HP-500-MO-OX gas purifier prior to use. Toluene was dried by refluxing over potassium and distilled prior to use. The absence of water and oxygen was confirmed by testing with a drop of potassium benzophenone radical solution in the glovebox. Dichloromethane was dried by refluxing over calcium hydride and distilled prior to use. Potassium bis(trimethylsilylamide), $K[N(SiMe_3)_2]$, was purchased from Sigma-Aldrich, dissolved in toluene at 90 °C and subsequently recrystallized at −35 °C. Pentamethylcyclopentadiene (HCp*) and H-2,5-dimethylpyrrole were purchased from Sigma-Aldrich and was dried over 4 Å sieves prior to use. Anhydrous rare earth chlorides ($RECl_3$, RE = Y, Gd, and Dy), 28–30% NH_4OH solution, and allylmagnesium chloride (2.0 M in THF) were purchased from Sigma-Aldrich and used as received. I_2 was purchased from Alfa-Aesar and purified by sublimation prior to use. H-pyrrole was purchased from Alfa-Aesar and dried over 4 Å molecular sieves prior to use. KCp* and K[DMP] were synthesized by deprotonation of HCp* and DMPH with $K[N(SiMe_3)_2]$, respectively.[29] A similar synthetic approach has been used for the synthesis of Li[DMP].[30] $Cp^*_2RE(\eta^3\text{-}C_3H_5)$ (RE = Y, Gd, and Dy) and $Cp^*_2RE(BPh_4)$ (RE = Y, and Dy) were prepared

according to literature procedures.[31,32] IR spectra were collected on solid crystalline samples with an Agilent Cary 630 FTIR spectrometer. UV-vis spectra were taken on an Agilent Cary 60 instrument, in 1 cm cuvette cells equipped with Schlenk adaptors. A PerkinElmer 2400 Series II CHNS/O analyser was used for CHN elemental analyses. All NMR spectra were recorded on a Bruker Avance NEO 500 MHz spectrometer in toluene-d_8. NMR samples were prepared under an argon atmosphere and sealed using J-Young tubes. Chloroform-d and DMSO-d_6 were purchased from Cambridge Isotope Lab. Toluene-d_8 was purchased from Sigma-Aldrich and was subsequently dried over a sodium–potassium alloy and filtered prior to use. Chloroform-d was dried over 4 Å molecular sieves prior to use.

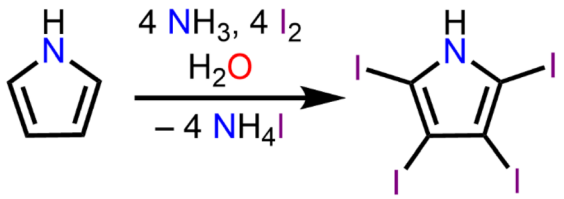

(1)

X-ray crystallography

Data were collected on a XtaLAB Synergy, Dualflex, HyPix diffractometer using Cu or Mo Kα radiation. Plate-shaped crystals with dimensions 0.2 × 0.14 × 0.06, 0.38 × 0.22 × 0.08, and 0.353 × 0.275 × 0.111 mm^3 for **1-Y**, **1-Gd**, and **1-Dy** and block-shaped crystals with dimensions of 0.524 × 0.329 × 0.196, and 0.283 × 0.174 × 0.138 mm^3 for **2-Y** and **2-Dy** respectively, were suspended in *n*-paratone oil and mounted on a nylon loop. The temperature was controlled using an Oxford Cryosystems low-temperature device. The structural refinement parameters for **1-RE** and **2-RE** are provided in Tables S1–S9.†

The data collection strategy, unit cell determination, and data reduction were performed by the CrysAlisPro software,[33] which corrects for Lorentz-polarization. Absorption effects were accounted for through use of a numerical absorption correction based on Gaussian integration over a multifaceted crystal model using spherical harmonics implemented in the SCALE3 ABSPACK[34] scaling algorithm.

The structure of **1-RE** and **2-RE** were solved in the space group $P2_1/c$ by using dual methods with the ShelXT[35] and refined by least squares using version 20189/2 of XL[36] incorporated in Olex2.[37] All non-hydrogen atoms were refined anisotropically. Hydrogen atom positions were calculated geometrically and refined using the riding model.

Synthesis of tetraiodopyrrole (TIPH)

The synthesis of TIPH was performed under aerobic condition (thus, without the precautions of an inert atmosphere) following a literature procedure, eqn (1).[38] 6.0 mL of 28–30% NH_4OH was diluted with 25 mL of H_2O and cooled to −78 °C in a 250 mL round bottom flask. To this, 667.0 mg (9.94 mmol) of H-pyrrole and 1.762 g (10.61 mmol) of KI was added. 10.112 g (39.83 mmol) of I_2 was dissolved in 75 mL of EtOH and added dropwise to the stirring pyrrole solution at −78 °C. The reaction was allowed to proceed under darkness at −78 °C. After 1 h, the light-brown reaction mixture was warmed up to room temperature and the product was precipitated by addition of 200 mL of H_2O and subsequently isolated by filtration. The crude solids were collected and dissolved in 12 mL EtOH. The ethanol solution was brought to a boil and 50 mg of activated charcoal was added. The mixture was allowed to heat for 1 h, and then filtered into a cold KI solution (0 °C, 207 mg, 1.25 mmol, 200 mL). The final product was isolated as a white solid from filtration of the KI/TIPH mixture in 30% yield (1.696 g, 2.97 mmol). Anal. calcd for C_4HNI_4: C 8.42, H 0.18, N 2.45. Found: C 8.71, H 0.31, N 2.46. ^{1}H (500 MHz, ppm, DMSO-d_6, 25 °C) δ 12.35 (s, 1H, $\underline{H}NC_4I_4$). ^{13}C (126 MHz, ppm, DMSO-d_6, 25 °C) δ 87.25 (NC_4H_4), 80.34 (NC_4H_4). (ATR, cm^{-1}) 3379s, 3360m, 2846w, 1469m, 1383m, 1333w, 1282m, 1224m, 1207w, 1005m, 941s, 911w, 842w.

Synthesis of $Cp^*_2Y(TIP)$, 1-Y

405.8 mg (1.01 mmol) of $Cp^*_2Y(C_3H_5)$ was dissolved in 3 mL of toluene in a 20 mL scintillation vial and subsequently, cooled to −78 °C. To this, 577.3 mg (1.01 mmol) of TIPH was added. The total volume of toluene was increased to 8 mL and the reaction was allowed to proceed at −78 °C, causing the initial yellow coloured mixture to turn green. After three hours, the green reaction was allowed to warm to room temperature, accompanied by the formation of a yellow-green precipitate. The toluene was removed under reduced pressure to yield a yellow-green solid. Yellow crystals of $Cp^*_2Y(TIP)$, **1-Y**, suitable for single-crystal X-ray diffraction analysis were obtained at −35 °C from a concentrated dichloromethane solution in 56% crystalline yield (575.4 mg, 0.57 mmol). **1-Y** crystallized with one CH_2Cl_2 molecule in the unit cell. ^{1}H NMR (500 MHz, ppm, chloroform-d, 25 °C) δ 2.00 (s, 30H, $C_5\underline{Me}_5$). ^{13}C NMR (126 MHz, ppm, chloroform-d, 25 °C) δ 121.48, ($\underline{C}_5Me_5$), 82.55, 82.33 (TIP), 12.23 ($C_5\underline{Me}_5$) Anal. calcd for $C_{24}H_{30}NI_4Y\cdot CH_2Cl_2$: C 29.61, H 3.18, N 1.38. Found: C 29.61, H 3.05, N 1.37. (ATR, cm^{-1}) 2898m, 1853m, 1429m, 1413w, 1377m, 1367w, 1356m, 1246w, 1213s, 1190s, 1163s, 1017m, 943s, 924s, 892w, 724s, 693s. Note for **1-Y**: the initial precipitation of the yellow-green solid during warm-up of the reaction from −78 °C to room temperature, was additionally isolated through centrifugation in one event for further investigation. The solid amounted to approximately 76% crude yield, and both ^{1}H NMR studies on the solid as well as single-crystals grown from this solid unambiguously have proven it to be **1-Y**.

Synthesis of $Cp^*_2Gd(TIP)$, 1-Gd

Following the synthetic procedure for **1-Y**, **1-Gd** (143.0 mg) was crystallized from dichloromethane solution at −35 °C in 43% crystalline yield (0.13 mmol). **1-Gd** is isostructural to **1-Y** and crystallized with one CH_2Cl_2 molecule in the unit cell. Used masses: $Cp^*_2Gd(C_3H_5)$ (140.9 mg, 0.30 mmol), TIPH (173.9 mg, 0.30 mmol). Anal. Calcd for $C_{24}H_{30}NI_4Gd\cdot CH_2Cl_2$: C 27.74, H 2.98, N 1.29. Found: C 27.60, H 3.00, N 1.30. (ATR, cm^{-1}) 2888m,

2851m, 1444m, 1414w, 1379m, 1366w, 1355m, 1261m, 1213s, 1180s, 1019m, 943s, 922s, 736s, 704s, 688s.

Synthesis of Cp*$_2$Dy(TIP), 1-Dy

Following the synthetic procedure for **1-Y**, **1-Dy** (251.0 mg) was crystallized as yellow crystals from dichloromethane solution at −35 °C in 47% crystalline yield (0.23 mmol). **1-Dy** is isostructural to **1-Y** and **1-Gd** and crystallized with one CH_2Cl_2 molecule in the unit cell. Used masses: Cp*$_2$Dy(C_3H_5) (231.8 mg, 0.49 mmol), TIPH (280.2 mg, 0.49 mmol). Anal. calcd for $C_{24}H_{30}NI_4Dy\cdot CH_2Cl_2$: C 27.61, H 2.97, N 1.29. Found: C 27.09, H 3.08, N 1.30. (ATR, cm^{-1}) 2892m, 2851m, 1429m, 1412w, 1377m, 1366w, 1354m, 1211w, 1189s, 1179s, 1162s, 1017m, 943s, 922s, 890w, 725s, 693s.

Synthesis of Cp*$_2$Y(DMP), 2-Y

In a 20 mL scintillation vial, 22.4 mg (0.16 mmol) of K[DMP] was added to a stirring 16 mL Et_2O solution containing 105.5 mg (0.16 mmol) of Cp*$_2$Y(BPh_4). After addition of K[DMP], 4 mL of Et_2O was added, increasing the total volume of the reaction to 20 mL. The reaction mixture was allowed to stir at room temperature for 1 h, concurrent with the production of a white precipitate, presumably $KBPh_4$. The cloudy reaction mixture was centrifuged, and the supernatant was filtered through a Celite plug. The toluene was removed under reduced pressure, yielding an oily solid which was redissolved in 4 mL of *n*-hexane. The resulting, yellow-coloured solution contained white particulates which were removed *via* filtration through a Kimwipe plug. All hexane was removed *in vacuo* give a crystalline solid. Yellow crystals of Cp*$_2$Y(DMP), **2-Y**, suitable for single-crystal X-ray diffraction analysis were grown from concentrated *n*-hexane solution at −35 °C in 42% crystalline yield (29.9 mg, 0.07 mmol). ^{1}H NMR (500 MHz, ppm, toluene-d_8, 25 °C) δ 1.79 (s, 30H, $C_5\underline{Me}_5$), 2.04 (s, 6H, $NC_4\underline{Me}_2H_2$), 6.26 (s, 2H, $NC_4Me_2\underline{H}_2$). $^{13}C\{^1H\}$ NMR (126 MHz, ppm, toluene-d_8, 25 °C) δ 120.45, ($\underline{C}_5Me_5$), 109.33 ($N\underline{C}_4Me_2H_2$), 108.04 ($N\underline{C}_4Me_2H_2$), 9.25–12.24 (q, $^1J_{C-H}$: 125.83 Hz, $C_5\underline{Me}_5$), 15.00–17.92 (q, $^1J_{C-H}$: 121.90 Hz, $NC_4\underline{Me}_2H_2$). Anal. calcd for $C_{26}H_{38}NY$: C 68.86, H 8.45, N 3.09. Found: C 68.48, H 8.81, N 3.05. (ATR, cm^{-1}) 3083w, 2965w, 2902m, 2858m, 2719w, 1484w, 1433m, 1373m, 1307w, 1254m, 1051w, 1021w, 949w, 745s.

Synthesis of Cp*$_2$Dy(DMP), 2-Dy

Following the synthetic procedure for **2-Y**, yellow crystals of **2-Dy** (23.4 mg, 0.04 mmol) were crystallized from *n*-hexane solution at −35 °C in 37% crystalline yield. Used masses: Cp*$_2$Dy(BPh_4) (64.0 mg, 0.09 mmol), K[DMP] (11.6 mg, 0.09 mmol). Anal. calcd for $C_{26}H_{38}NDy$: C 59.25, H 7.27, N 2.66. Found: C 58.92, H 7.66, N 2.65. (ATR, cm^{-1}) 3081w, 2964w, 2901m, 2855m, 2718w, 1486w, 1432m, 1371m, 1305w, 1253m, 1051w, 1020w, 948w, 743s.

Magnetic measurements

Magnetic data were collected on a Quantum Design MPMS3 SQUID magnetometer. Polycrystalline Cp*$_2$Gd(TIP) (**1-Gd**), Cp*$_2$Dy(TIP) (**1-Dy**), and Cp*$_2$Dy(DMP) (**2-Dy**) were first dried under high vacuum, and then 25.3 mg (0.02 mmol), 16.8 mg (0.02 mmol) and 12.3 mg (0.02 mmol) respectively, were immobilized with molten eicosane (60 °C) prior to the experiment. After ensuring an airtight seal, the sample was transferred out of the glovebox and mounted onto the SQUID sample holder.

Dc magnetic susceptibility data were collected at temperatures ranging from 2 to 300 K. Ac magnetic susceptibility data were collected under a 3 Oe oscillating magnetic field. All data were corrected for diamagnetic contributions from the eicosane and core diamagnetism estimated using Pascal's constants.[39] The molar masses used to work up the raw magnetic data for all compounds are based on the molar mass determined by single-crystal X-ray diffraction study and matching elemental analysis.

Continuous wave electron paramagnetic resonance spectroscopy

Continuous-wave X-band EPR spectra were recorded at 5 K using a Bruker Elexsys E500 spectrometer. Temperature control was provided by a Lakeshore temperature controller and an ESR 900 cryostat in combination with a ColdEdge Stinger system. All simulations of EPR spectra were performed using EasySpin.[40]

Computational methods

The pK_a values of H-tetraiodopyrrole, H-pyrrole, and H-2,5-dimethylpyrrole were evaluated based on a theoretical proton transfer reaction between the protonated heterocycle and one water molecule using the computational derived thermodynamic parameters. The effectiveness of this method has previously been shown in a series of carboxylic acids.[41] H-tetraiodopyrrole, H-pyrrole, H-2,5-dimethylpyrrole, H_2O, and H_3O^+ were calculated at the def2-TZVP level,[42] retrieved through Basis Set Exchange,[43] employing the CAMB3LYP functional.[44] A 28 electron in-core pseudo potential was used for the iodine substituents of the TIP ligand.[45] To account for the effects of solvation, a CPCM (H_2O) solvent model was included.[46,47] Further details are provided in the ESI.†

The electronic structure of **1-Y** and **2-Y** were studied by density functional theory (DFT) calculations through use of the Gaussian software suite.[48] A suitable functional for the characterization of **1-Y** and **2-Y** was determined through comparison of the experimental and computed bond metrics of various functionals employing the def2-SVP basis set, Tables S26, S27 and S30, S31.†[42,49] It was determined that the hybrid meta-GGA functional TPSSh, most accurately described the structure of **1-Y**, and thus, a final geometry optimization was performed using the larger def2-TZVP functional on all atoms, as well as a 28 in-core electron pseudopotential (ECP28MDF[45]) and GD3 (ref. 50 and 51) empirical dispersion correction on both the central Y ion, as well as the ancillary iodine substituents. TDDFT calculations were conducted on the optimized structure of **1-Y** for 50 excited states on the def2-TZVP/ECP28MDF(Y,I) level of theory using the TPSSh functional with GD3 dispersion correction. A CPCM implicit solvent model for dichloromethane was included.[46,47] In the case of **2-Y**, multiple

functionals accurately predicted the experimentally determined geometry, Tables S30 and S31.† Owing to the success of the TPSSh functional in the optimization of **1-Y**, the final geometry of **2-Y** was also completed using this description. Final optimizations were performed employing the very-tight optimization criteria. The minimum structures were confirmed through analytical frequency calculations. One small, imaginary frequency (10i cm^{-1}) was found for **1-Y**, owing to the flat potential energy surface regarding the rotation of the $[Cp^*]^-$ ligands. This phenomenon has also been observed in similar RE metal organometallic complexes, and is considered benign if the frequency in question does not concern the atoms of interest.[52] The bonding situation of **1-Y** and **2-Y** were investigated through a natural localized molecular orbital (NLMO)[53] analysis, at def2-TZVP/ECP28MDF(Y,I) level of theory using the TPSSh functional with GD3 dispersion correction. The relevant donor/acceptor NLMO interactions are provided in Tables S29 and S32,† respectively. Only strongest interactions between the pyrrolyl ligand and metal ion are depicted (>1 kcal mol^{-1}).

The magnetic properties of **1-Dy** and **2-Dy** were calculated *via* a complete active space self-consistent field (CASSCF) +N-valence perturbation theory (NEVPT2) approach implemented in the ORCA 5.0.4 package.[54,55]

Results and discussion

Synthesis and structural characterization

The development of materials featuring non-covalent interactions is currently of large interest given the desire to promote stability and the appearance of unique physical and chemical properties of new crystal forms. Halogen bonding, a subset of the σ-hole interactions, is particularly intriguing as many covalently bonded halogens have regions of positive electrostatic potential along the axes of the covalent bond.

To implement these interactions into crystals containing bis-cyclopentadienyl scaffolds containing rare-earth centres, we turned to the halogenated heterocycle 2,3,4,5-tetraiodopyrrole. Complexes innate to tetraiodopyrrole ligands are unknown, rendering them intriguing synthetic targets for the development of new multifunctional materials. The synthesis of 2,3,4,5-tetraiodopyrrole (TIPH) was first described in 1882,[25] eqn (1), and has since been investigated in the development of building blocks for halogen bond-assisted supramolecular structures.[23]

The installation of RE metallocene units into larger molecules benefits from the isolation of materials that have prolific use in various applications such as in catalysis and magnetism.[56,57] An attractive synthetic strategy utilizes allylic complexes $Cp^*_2RE(\eta^3\text{-}C_3H_5)$, where the allyl component can readily extrude the relatively inert propene gas by adding an acidic proton. The use of this particular driving force has been demonstrated for RE and other early transition metals giving rise to both mono- and multi-nuclear complexes including, $Cp^*_2Y(NH_2)THF$, $[Cp'_2Zr(\mu^3\text{-}S)DyCp^*_2]_2$, $[Cp^*_2Dy(\mu\text{-}CNC_6H_4O\text{-}\kappa C{:}\kappa O)]_2$,[58] $[((\eta^5\text{-}Cp^*)_2RE)_2(\mu\text{-}1\eta^2\text{-}pyr\text{-}2\kappa N)(\mu\text{-}2\eta^2\text{-}pyr\text{-}1\kappa N)]$,[59] and dinuclear complexes in the presence of H_2.[60,61]

Capitalizing on this fruitful synthetic approach, the bis(-pentamethylcyclopentadienyl) RE tetraiodopyrrole complexes

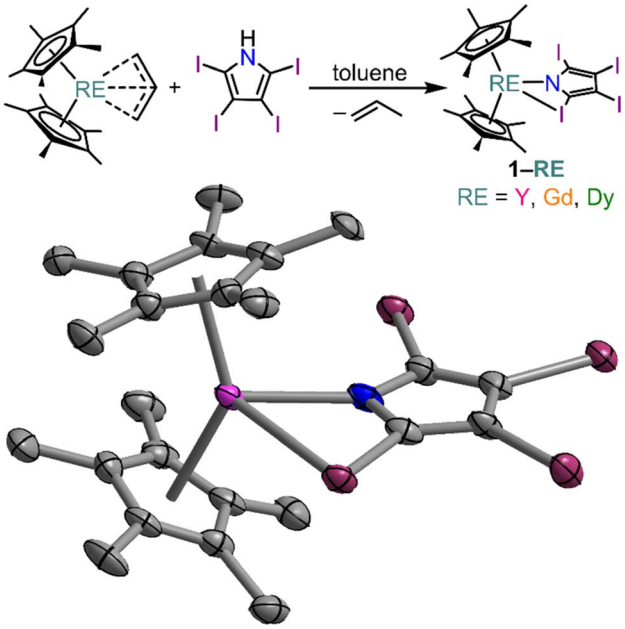

Fig. 2 Synthetic scheme (upper) and structure of $Cp^*_2Y(TIP)$, **1-Y**, (lower), with thermal ellipsoids drawn at 50%. Pink, purple, blue, and grey ellipsoids represent Y, I, N, and C atoms, respectively. Hydrogen atoms and co-crystallized dichloromethane have been omitted for clarity. Selected interatomic distances (Å) and angles (°): Y–N = 2.367(6); Y–I = 3.238(1); Y···C_{C2} = 3.128(7); Y–Cnt = 2.355 and 2.344; Cnt–Y–Cnt = 139.4; Gd–N = 2.410(3); Gd–I = 3.253(1); Gd···C_{C2} = 3.164(4); Gd–Cnt = 2.391 and 2.390; Cnt–Gd–Cnt = 139.9; Dy–N = 2.376(3); Dy–I = 3.233(1); Dy···C_{C2} = 3.130(3); Dy–Cnt = 2.357 and 2.359; Cnt–Dy–Cnt = 139.3.

$Cp^*_2RE(TIP)$, **1-RE**, (RE = Y (**1-Y**), Gd (**1-Gd**), and Dy (**1-Dy**)) were isolated from a protonolysis reaction of H-tetraiodopyrrole and the respective RE allyl complexes in toluene, Fig. 2. Notably, **1-RE** is poorly soluble in toluene, causing it to precipitate as a yellow-green solid as the reaction progresses (where the isolated solid amounted to approximately 76% crude yield for **1-Y**). Yellow crystals suitable for single-crystal X-ray diffraction analysis were grown from concentrated dichloromethane solution at −35 °C in 56, 43, and 47% crystalline yields, for **1-Y**, **1-Gd**, and **1-Dy**, respectively. All three complexes are isostructural and crystalize in the space group $P2_1/c$ with four molecules in the unit cell, Fig. S8.† In all cases the first coordination sphere of the eight-coordinate metal centre is comprised of two pentamethylcyclopentadienyl ligands, the nitrogen and one iodine atom of the TIP ligand.

In order to assess the influence of the ancillary iodine atoms we pursued the synthesis of an all-hydrocarbon alternative in the first coordination sphere. For this, we turned to 2,5-dimethylpyrrole (DMPH). Here, the differing substitution has a dramatic influence on the basicity of the N-atom of the heterocycle. In order to estimate the pK_a of the TIPH, pyrrole, and DMPH ligands, we computationally determined the thermodynamic parameters for the proton transfer reaction between the heterocycle and one water molecule. This approach has been described in the estimation of pK_a for several carboxylic acids.[41,62] The relevant thermodynamic values are provided in Tables S24 and S25,† resulting in estimated pK_a

values of 6.19, 21.10, and 23.45 for TIPH, H-pyrrole, and H-2,5-dimethylpyrrole respectively. Interestingly, when DMPH is reacted directly with $Cp^*_2RE(\eta^3\text{-}C_3H_5)$ no reaction is observed likely because of the decreased acidity of the N-proton.

Thus, we pursued an alternative synthetic approach to isolate the unprecedented $Cp^*_2RE(DMP)$ (RE = Y (**2-Y**) and Dy (**2-Dy**), DMP = 2,5-dimethylpyrrolyl), which were obtained from salt-metathesis reactions of $Cp^*_2RE(BPh_4)$ (RE = Y, Dy) and the potassium salt of 2,5-dimethylpyrrolyl, K[DMP], Fig. 3. Similar approaches have been employed to implement the $[Cp^R_2RE]^+$ cation (where R = alkyl) to obtain both mono- and multinuclear RE compounds.[31,63–69] Notably, we recently extended this approach to systems bearing guanidinate anions.[70,71] Recently, both guanidinate and the structurally and electronically related amidinate ions have been shown to be attractive ligands for the design of single-molecule magnets.[70,72–75] Yellow single-crystals of **2-RE** were grown from concentrated *n*-hexane solutions at −35 °C in 42 and 37% crystalline yield for **2-Y** and **2-Dy**, respectively. **2-RE** are isostructural and crystalize in the monoclinic space group $P2_1/c$ akin to **1-RE**. The structure of **2-RE** is topologically similar to that of **1-RE** as each metal centre is seven-coordinate and ligated by two pentamethylcyclopentadienyl anions and one asymmetrically coordinated DMP substituent with one main interaction to the nitrogen atom, and two weak agostic interactions to one of the methyl groups of the pyrrole ring, and the adjacent C2 carbon of the pyrrole ring.

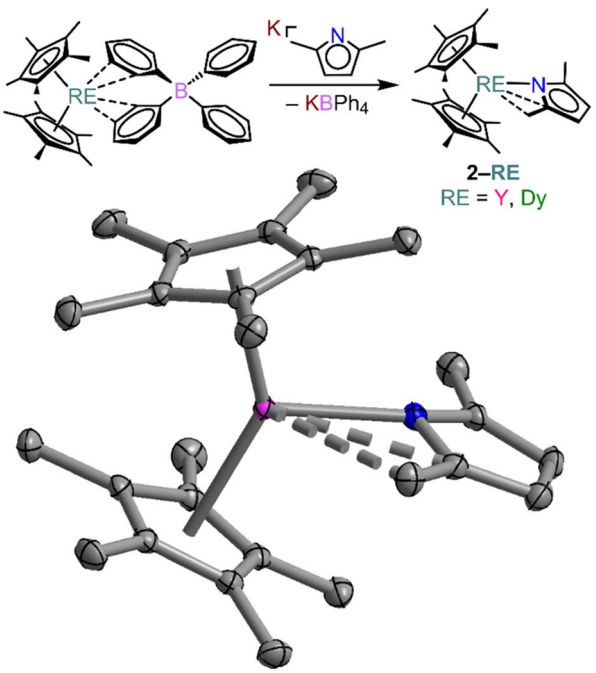

Fig. 3 Synthetic scheme (upper) and structure of $Cp^*_2Y(DMP)$, **2-Y**, (lower), with thermal ellipsoids drawn at 50%. Pink, blue, and grey ellipsoids represent Y, N, and C atoms, respectively. Hydrogen atoms have been omitted for clarity. Selected interatomic distances (Å) and angles (°): Y–N = 2.289(1); $Y–C_{Me}$ = 2.993(2); $Y–C_{C2}$ = 2.983(2); Y–Cnt = 2.342 and 2.388; Cnt–Y–Cnt = 139.5; Dy–N = 2.299(2); $Dy–C_{Me}$ = 2.996(2); $Dy–C_{C2}$ = 2.987(2); Dy–Cnt = 2.347 and 2.341; Cnt–Dy–Cnt = 139.7.

Excitingly, **1-RE** represent the first report of tetraiodopyrrole as a ligand for any metal ion. Notably, the σ- and π-type Lewis basicity of pyrrolyl ligands allows a wide range of coordination modes from η^1–η^5.[76] Recently, the first report of an η^1:η^2-bridging coordination mode of the pyrrolyl ligand was reported by some of us, resulting from a highly strained dinuclear complex.[59] However, in both **1-RE** and **2-RE**, the N-atom of the pyrrolyl ligand forms a σ-type interaction with the metal centre, without any additional interactions arising from the π-system. Notably, the RE–N interaction in **1-RE** is significantly elongated with 2.367(6), 2.410(3) and 2.376(3) Å for **1-Y**, **1-Gd**, and **1-Dy**, respectively, compared to 2.289(1) and 2.299(2) Å for **2-Y** and **2-Dy**, respectively. This is attributed to the significant differences in basicity of the coordinating nitrogen atom in TIP *vs.* DMP. The small differences in interatomic distances across isostructural complexes are attributed to the slight variations in ionic radii for Y, Gd, and Dy (Y^{III} = 1.019, Gd^{III} = 1.053, and Dy^{III} = 1.027 Å; CN = 8).[77] Remarkably, neither pyrrolyl ligand coordinates symmetrically to the metal centre. In both cases, one substituent in the 2-position of the heterocyclic ring lies substantially closer to the metal than the other. The shortest interatomic RE–I distances in **1-RE** ($RE–I^1$) amount to 3.238(1) (**1-Y**), 3.253(1) (**1-Gd**), and 3.233(1) (**1-Dy**) Å, hinting at a significant metal iodine interaction, see Fig. S7† for relevant atom labels. These interatomic distances are significantly longer than other complexes bearing direct Dy–I bonding interactions such as $(NN^{TBS})DyI(THF)_2$,[78] (NN^{TBS} = $Fc(NHSi^tBuMe_2)_2$; Dy–I = 3.09 Å), $Cp^*_2DyI(THF)$,[79] (Dy–I = 2.982 Å), and $Dy(Cy_3PO)_3I_3$ (Dy–I = 3.055–3.097 Å).[80] In contrast, the nearest methyl substituent of the DMP ligand in **2-RE** resides significantly closer to the metal centre, with distances of 2.993(2) and 2.996(2) Å in **2-Y** and **2-Dy**, respectively. The Cnt–RE distances in **1-RE** (where Cnt centroid of the pentamethylcyclopentadienyl ring) are 2.355 and 2.344 Å for **1-Y**, 2.391 and 2.390 Å for **1-Gd**, and 2.357 2.359 Å for **1-Dy**. By contrast, the respective Cnt–RE distances in **2-RE** are marginally shorter with 2.342 and 2.338 Å for **2-Y**, and 2.347 and 2.341 Å for **2-Dy**. For both set of compounds, the ∠Cnt–RE–Cnt metallocene angle is slightly larger than 131.8° found in $[Cp^*_2Y(\mu\text{-pyr})]_2$ (139.4°, 139.3°, 139.9°, 139.5°, and 139.7° for **1-Y**, **1-Dy**, **1-Gd**, **2-Y**, and **2-Dy**, respectively).

Intriguingly, the closest intermolecular I···I interaction is 3.838(1) Å, observed in **1-Y**, which is approximately 0.15 Å less than the van der Waals radii for two I atoms (3.98 Å).[81] In addition to the reduced I···I interatomic distance, another key observable of a σ-hole interaction is the interatomic distance between the C and halogen substituent.[82] A σ-hole interaction typically changes the length of the C–I covalent bond that is colinear with the σ-hole interaction by ±0.03 Å or less.[83–85] The C–I interatomic distances in free TIPH range from 2.060(6) to 2.054(6) Å,[38] which is 0.039 Å shorter than the $C–I^1$ distance of 2.099(8) Å observed in **1-Y**. Typically, halogen···halogen interactions are separated into two types: type I and type II.[82] There are clear chemical and geometric criteria for the designation of which classification is most appropriate for a given interaction.[82] Interactions of type I are typically geometry-based and arise from close crystal packing, which are observed for all halogen atoms. By contrast, type II interactions originate from

electrophile-nucleophile pairings, which is a direct consequence of the increased polarizability of the I atom. Since the region of positive electrostatic potential lies along the same axis of the covalent bond, the σ-hole interaction is normally colinear with the covalent C–I bond. For **1-Y**, the ∠C–I–I angle is 166.5(2)°, where the deviation from linearity is attributed to crystal-packing affects.

In general, weak interactions with shallow potential energy wells do not cost much energy, thus have large deformation with changing temperatures. Notably, the interatomic distances of halogen bonding interactions are extremely dependent on temperature.[28] To probe the temperature dependence of the structure of the complex in the solid state, a single-crystal X-ray diffraction analysis of **1-Dy** was conducted at varying temperatures from 100 to 300 K, Fig. 4, S5 and S6.† The monotonic changes in unit cell dimensions, Fig. 5, preclude any potential phase transition over the probed temperature range. Traversing the temperature from 100 to 300 K, the unit cell parameters for **1-Dy** elongate ($\Delta a = 0.1106$ Å, $\Delta b = 0.1754$ Å, and $\Delta c = 0.3346$ Å) causing an expansion of 3.6% for the unit cell volume (compare V = 3058.4(1) and 3168.2(2) Å^3 for 100 and 300 K, respectively). Over the entire probed temperature range, the TIP ligand maintains a κ^2-coordination mode, Fig. 4. Noteworthy, the Dy–I^1 interatomic distance increases substantially (ΔDy–I^1 = 0.024 Å), Fig. 5B, whereas the Dy–N interatomic distance remains unchanged, as it relates to the magnitude of the standard deviation, Fig. S9.† The displacement of the coordinated iodine atom is also observed in the I^1–I^2 interatomic distance, Fig. 5C, which declines substantially with increasing temperature. In addition, the N–C and C–C distances around the pyrrole ring remain invariant as a function of temperature, suggesting that this phenomenon is localized to the ancillary I-substituents, Fig. S10.†

Several description of halogen bonding have been developed, including those based on the natural orbitals of chemical valence (ETS-NOCV), which provides a quantitative picture of the electronic and electrostatic influences at play between donor and acceptor units.[86] One description of intermolecular halogen···halogen bonding invokes molecular orbital theory along the X···X axis.[21] Due to the energy lowering arising from the favourable orbital overlap between the two halogen substituents, the formation of both a formally bonding and antibonding molecular orbital is observed.[87] Notably, the closest intermolecular I···I interaction (I^1–I^3) monotonically increases from 3.838(1) to 3.980(1) Å (ΔI^1–I^3 = 0.142 Å) with elevating temperature, Fig. S11,† consistent with the population of the σ*-LUMO with increasing temperatures. The same scenario is found for the second closest intermolecular I···I interaction (I^1–I^4), Fig. S12,† which increases from 4.374(1) Å to 4.535(1) Å (ΔI^1–I^4 = 0.161 Å). Notably, instead of the linear growth in intermolecular interatomic distance observed for the other I···I interactions, the I^3–I^3 distances display a parabolic behaviour, Fig. S13,† likely owing to the colinear orientation of the σ-hole relative to the halogen···halogen interaction.

Magnetic studies

Dc magnetic susceptibility (χ_M) data for **1-Gd**, **1-Dy**, and **2-Dy** were collected from 2 to 300, Fig. 6 and S36–S38.† At 1.0 T the room temperature $\chi_M T$ values 7.43, 15.27 and 14.96 cm^3 K mol^{-1} for **1-Gd**, **1-Dy** and **2-Dy**, respectively, are in good agreement with the expected values of 7.88 cm^3 K mol^{-1} and 14.14 cm^3 K mol^{-1} for the unperturbed Gd^{III} and Dy^{III} ions, respectively. The higher $\chi_M T$ value for the dysprosium congeners may be attributed to a combination of higher magnetic anisotropy,[88] and a slight discrepancy in mass.

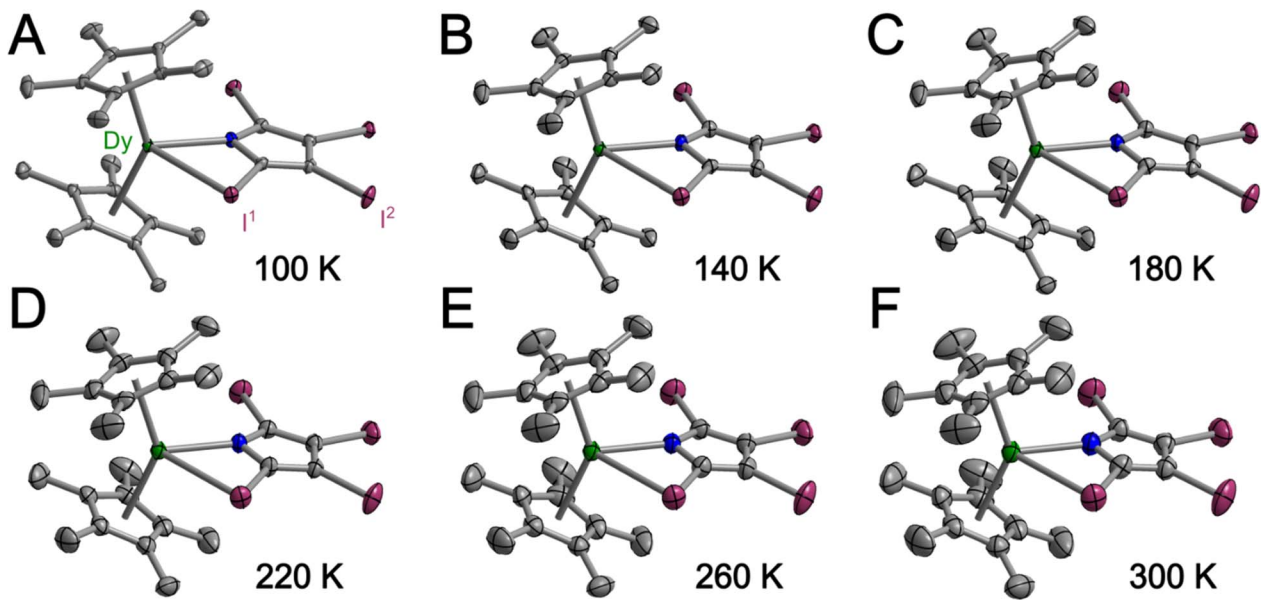

Fig. 4 Structure of **1-Dy** in a crystal of $Cp^*_2Dy(TIP)\cdot CH_2Cl_2$ with thermal ellipsoids drawn at 50% at 100 K (A), 140 (B), 180 (C), 220 (D), 260 (E) and 300 K (F), respectively. Green, purple, blue, and grey ellipsoids represent Dy, I, N, and carbon atoms respectively. H atoms and co-crystallized dichloromethane are omitted for clarity.

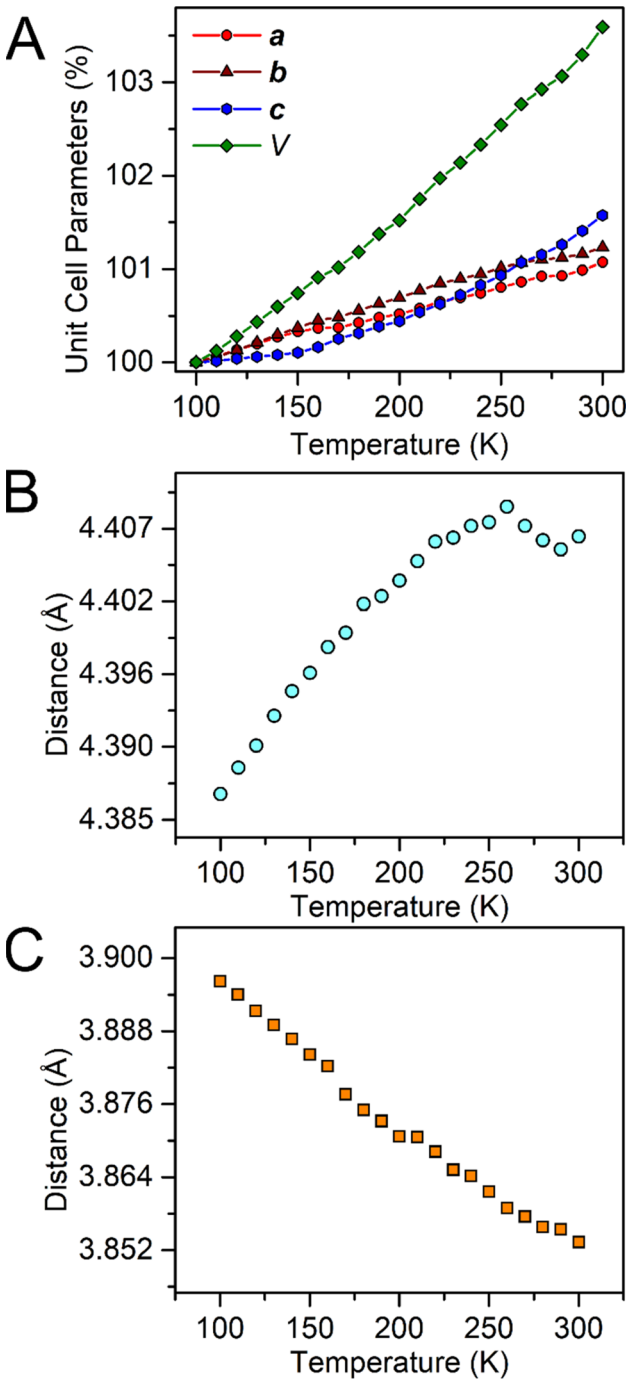

Fig. 5 Plots of the temperature dependence of the unit cell parameters (A), and interatomic Dy–I^1 (B), and I^1–I^2 (C) distances of Cp*$_2$-Dy(TIP)·CH_2Cl_2. The error bars are within the radius of the symbols. Please see Fig. S7† for relevant atom labels. Graphical representations of the intermolecular halogen···halogen interactions are provided in Fig. S11–S13.†

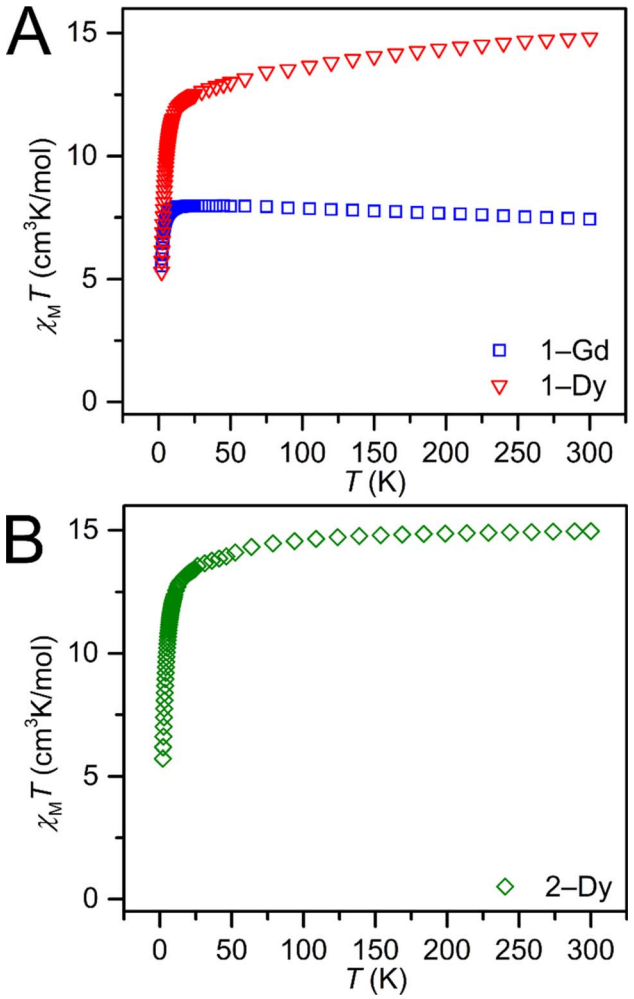

Fig. 6 Variable-temperature dc magnetic susceptibility data ($\chi_M T$ *vs. T)* of polycrystalline Cp*$_2$RE(TIP) (RE = Gd (**1-Gd**), and Dy (**1-Dy**)) and polycrystalline Cp*$_2$Dy(DMP) (**2-Dy**), collected under a 1.0 T applied dc field.

As the temperature is lowered, a slight decline in $\chi_M T$ is observed until 13.0 and 14.2 K, respectively, for **1-Dy** and **2-Dy**. At the lowest temperatures, a sharp drop in $\chi_M T$ occurs, in accordance with the depopulation of the Stark sublevels of the Dy^{III} ion.[89] The field- and zero-field-cooled magnetic susceptibility data of both **1-Dy** and **2-Dy** are superimposable, indicating the absence of magnetic blocking. The field-dependent magnetization data of **1-Gd**, **1-Dy**, and **2-Dy** were collected between 2 and 10 K. For the Dy^{III} complexes, magnetic saturation was not reached even at 7 T. At 2 K, the magnetization grows with increasing magnetic field until it reaches a value of 5.82 and 6.09 Nμ_B, slightly higher than the expected saturation magnetization for one Dy^{III} ion (5.23 Nμ_B), suggestive of the presence of significant magnetic anisotropy.[90] Similarly, at 2 K the magnetization of **1-Gd** grows with increasing applied field until it reaches a value of 7.56 Nμ_B. The reduced magnetization curves (*H*/*T versus M*) for **1-Dy** and **2-Dy** at temperatures ranging from 2 to 10 K are non-superimposable, indicative of thermally accessible excited states, Fig. S50 and S60.†[89]

A single Dy^{III} ion is a Kramers' ion and innate to high magnetic anisotropy, which can be augmented by pairing it with an appropriate ligand field, ushering in single-molecule magnet behaviour.[91] Multinuclear SMMs featuring real magnetic memory require strong magnetic exchange coupling between multiple lanthanide centres due to the deeply contracted nature of the 4f-orbitals. Strong coupling ensures the emergence of a giant spin

which helps suppressing quantum tunnelling of the magnetization (QTM) and thus, engendering slower magnetic relaxation. Several strategies to foster strong coupling has been proven to be successful: (1) metal–metal bonding interactions,[92] (2) radical-bridging ligands with diffuse spin orbitals,[31,64,66,93] and (3) diamagnetic heavy main group element-containing bridges, also innate to diffuse orbitals, capable of penetrating the core-like 4f-mainfold.[94,95] Notably, the inclusion of heavy main-group elements into the primary coordination sphere of a given metal ion influences the zero-field splitting parameter,[88,96,97] owing to the $\sim Z^4$ dependence on the spin–orbit coupling Hamiltonian.[98] With this in mind, the dynamic magnetic properties of both **1-Dy** and **2-Dy** were explored under zero dc field, Fig. S39, S40 and S53.† **1-Dy** displays out-of-phase (χ_M'') components of the ac magnetic susceptibility from 1.8 to 14 K. The position of the signals hinges marginally on temperature and move past 1000 Hz at temperatures above 14 K. Relative to some other neutral, mononuclear SMMs containing a dysprosium metallocene unit,[99,100] the χ_M'' signals move faster which originates from more prevalent quantum tunnelling of the magnetization (QTM), potentially arising from the asymmetric crystal field imparted by the coordinated TIP ligand relative to that of the neutral ammonia or large $[BPh_4]^-$ anion. Employing the Cole–Davidson model implemented in CCFit2 to extract relaxation times yielded seemingly satisfactory fits,[48,49] however, with large standard deviations attributed to the high frequency χ_M'' peak position.

For **2-Dy**, the peak maximum of the out-of-phase (χ_M'') component of the ac magnetic susceptibility resides past the frequency limit of the magnetometer at 2 K and the peak loses intensity with raising temperature up to 10 K, thus precluding the extraction of relaxation times, Fig. S53.†

The application of an external magnetic field can mitigate these fast relaxation pathways. To determine the optimum field, out-of-phase ac susceptibility χ_M'' was collected at 2 K under dc fields ranging from 250 to 1500 Oe (**1-Dy**) and 250 to 1550 Oe (**2-Dy**), Fig. S42 and S54,† respectively. In both cases, the exposure to external magnetic fields influences the shape of the χ_M'' signals. Subjecting to strong magnetic fields decreases substantially the intensity of the peaks positioned at higher frequency, concurrent with the appearance of signals at lower frequency. The optimum dc fields are 1250 Oe for **1-Dy** and 1450 Oe for **2-Dy** as the high-frequency peak at these fields vanished entirely. Thus, variable-temperature ac susceptibility measurements of **1-Dy** and **2-Dy** were performed at these dc fields which uncovered much stronger temperature dependences than were apparent under zero dc fields.

Temperature-dependent χ_M'' peaks were observed for **1-Dy** between 4.5 and 26.5 K under a 1250 Oe applied dc field, Fig. 7A. Using the program CCFit[101] the relaxation times (τ) were extracted from a generalized Debye model from the generation of Cole–Cole plots, Fig. S45,† and were subsequently used to construct an Arrhenius plot. A satisfactory fit of the relaxation times was achieved through considering a Raman process utilizing the eqn (2)

$$\frac{1}{\tau} = CT^n \qquad (2)$$

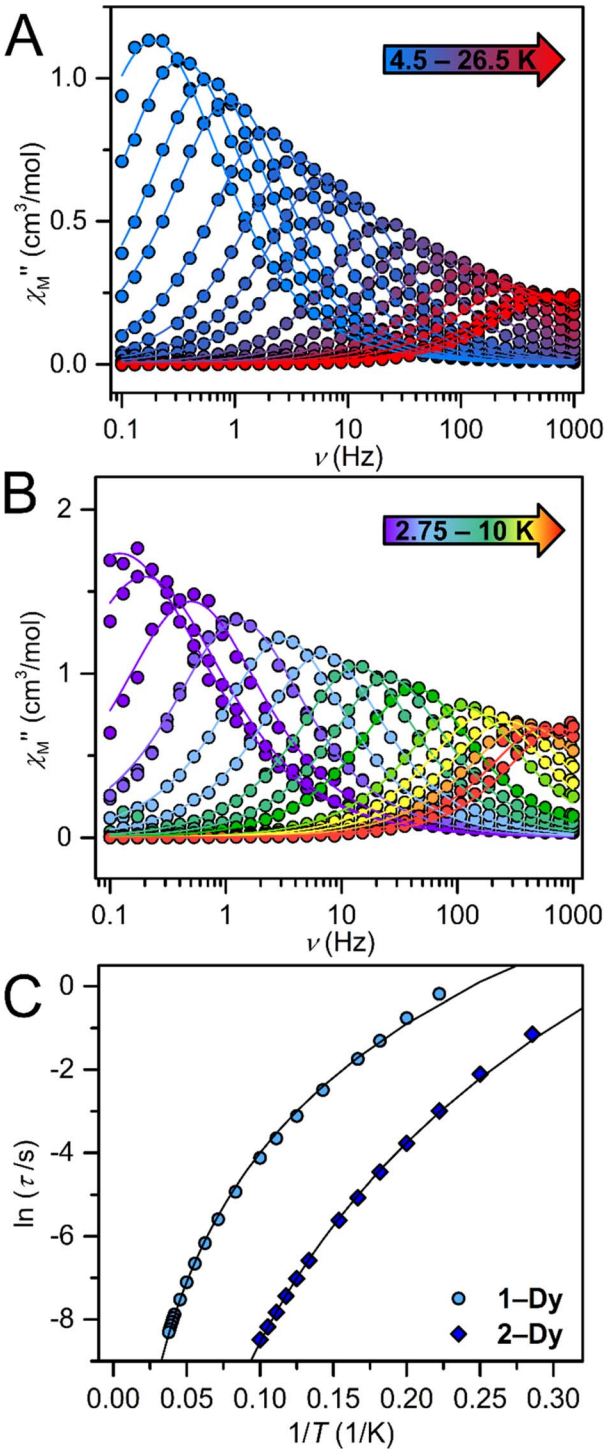

Fig. 7 (A) Out-of-phase (χ_M'') components of the ac magnetic susceptibility for Cp*$_2$Dy(TIP), **1-Dy**, under a 1250 Oe applied dc field from 4.5 K (blue) to 26.5 K (red). (B) Out-of-phase χ_M'' components of the ac magnetic susceptibility for Cp*$_2$Dy(DMP), **2-Dy**, under a 1450 Oe applied dc field from 2.75 K to 10 K. (C) Arrhenius plots of the natural log of the relaxation times, τ, *vs.* the inverse temperatures, 1/T, obtained from ac measurements for **1-Dy** (circles) and **2-Dy** (diamonds) at 1250 and 1450 Oe respectively. The best fits were obtained by considering a Raman process yielding $C = 0.0018(2)$ s^{-1} K^{-n}, $n = 4.48(3)$ and $0.00062(5)$ s^{-1} K^{-n}, $n = 6.92(4)$ for **1-Dy** and **2-Dy**, respectively.

The temperature-dependent out-of-phase χ''_M signals of **2-Dy** occur between 2.75 and 10 K at 1450 Oe dc field, Fig. 7B. Similarly, through the generation of Cole–Cole plots, Fig. S57,† the relaxation times were extracted using a generalized Debye model as implemented in CCFit2.[101] The resulting experimentally determined relaxation times were subsequently fit to a Raman process yielding $C = 0.00062(5)\ s^{-1}\ K^{-n}$, $n = 6.92(4)$, Fig. 7C.

The retention of magnetization in the absence of an applied dc magnetic field is a key observable for any SMM. Variable-field magnetization measurements were conducted on **1-Dy** at ±7 T from 1.8 to 4 K, Fig. S51 and S52.† At the lowest temperatures, the variable-field magnetization data displays a slightly open butterfly hysteresis loop, where the coercivity of $H_c = 0.18$ T exceeds the sweep rate of 100 Oe at its largest point. The magnetic hysteresis measurement conducted on **2-Dy** lacks coercivity at the lowest temperature measured, Fig. S61.†

Electron paramagnetic resonance (EPR) spectroscopy

Since the introduction of heavy main-group elements into the first coordination sphere of the paramagnetic metal ion impacts the zero-field splitting parameter with respect to the transition metals,[88,96,97] we set out to probe the influence of the proximal I-atom on the cw-EPR spectrum of **1-Gd**. The spin-only Gd^{III} ion can give rise to well-resolved EPR signals, unlike other paramagnetic lanthanides that oftentimes lead to non-informative EPR peaks that are weak or silent altogether.[102] The ^8S ground state of the Gd^{III} ion is separated by ~35 000 cm^{-1} from the first excited state (^6P).[103] The EPR spectrum of a well-isolated spin ground state can be described in terms of the following spin Hamiltonian, eqn (3).

$$\hat{H}_s = D\left[\hat{S}_z^2 - \frac{S(S+1)}{3} + \frac{E}{D}\left(\hat{S}_x^2 - \hat{S}_y^2\right)\right] + \beta_e \vec{B}\cdot\tilde{g}\cdot\hat{S}. \quad (3)$$

The first term is the zero-field splitting (ZFS) interactions. Here, $\hat{S}_\mu$ is the component of the spin operator ($\mu = x, y, z$) and D/E are the axial and rhombic terms of the ZFS, respectively. In cases where $S \geq 2$, the spin system may need to be characterized by higher order ZFS terms.[104] We have limited the analysis to only second-order terms as not to overparameterize the model. The second term is the electronic Zeeman interaction where β_e is the electron Bohr magneton, $\vec{B}$ is the magnetic field vector, $\tilde{g}$ is the g-tensor (assumed to be isotropic), and $\hat{S}$ represents the electron spin operator.

Our best simulations for the spectrum, Fig. 8 and Table S10,† recorded at 5 K of **1-Gd** require E/D to be near 1/3 with $D = -0.121\ cm^{-1}$, $|E| = 0.039\ cm^{-1}$ ($|E/D| = 0.322$), and $g_{iso} = 1.992$. A second spectrum recorded at 100 K required slightly different parameters to simulate. The necessity for different parameters is best appreciated by comparing the ~2 mT shift in the lowest field resonance (~0.05 T) and the splitting of the second lowest field feature near 0.09 T. We find that both observations can be reproduced by using $D = -0.122$, $|E| = 0.037\ cm^{-1}$ ($|E/D| = 0.304$), and $g_{iso} = 1.992$.

These values are very similar to those observed for the metallocenium complex $[Cp^{ttt}{}_2Gd][B(C_6F_5)_4]$ ($Cp^{ttt} = C_5H_2{}^tBu_3$-1,2,4) ($D = -0.1937\ cm^{-1}$ and $|E| = 0.0148\ cm^{-1}$) indicative of substantial axial ZFS.[105] Notably, the halogenated species, $Cp^{ttt}{}_2Gd(Cl)$ yields a more rhombic signal ($D = 0.0920\ cm^{-1}$ and $|E| = 0.0239\ cm^{-1}$).

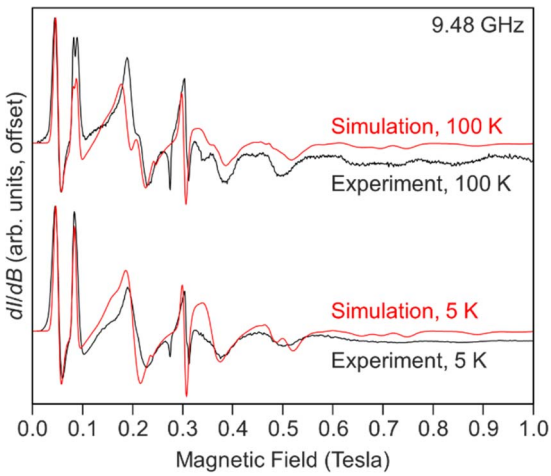

Fig. 8 Experimental (black) and simulated (red) X-band EPR spectra of $Cp^*{}_2Gd(TIP)$, **1-Gd** recorded at 5 (bottom) and 100 (top) K.

Electronic absorption spectroscopy

Electronic absorption spectra of **1-RE** were taken in dichloromethane, Fig. 9, S34.† The complexation of the tetraiodopyrrole ligand results in the emergence of a band at ~350 nm. For all compounds, there is minor change in the absorption spectra across the series. Notably, the UV-vis spectrum of the Gd complex features the emergence of a band centred at 411 nm. To gain insight into the electronic absorption spectra of **1-Y**, TDDFT calculations were carried out, Table S28.† The most

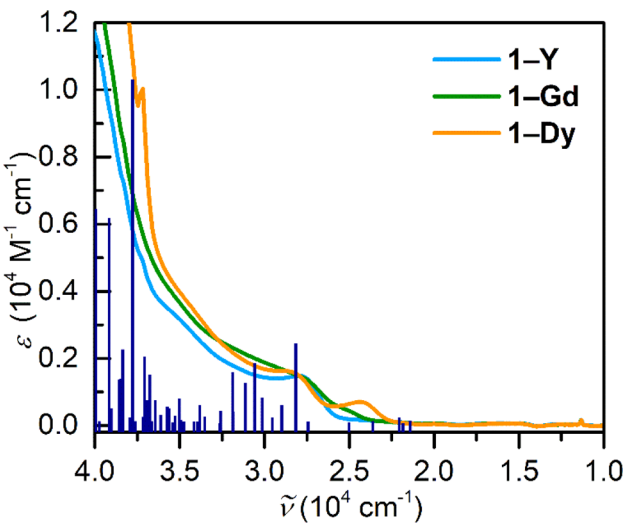

Fig. 9 UV-vis absorption spectrum of $Cp^*{}_2RE(TIP)$ (RE = Y (**1-Y**), Gd (**1-Gd**), and Dy (**1-Dy**)) in dichloromethane solution. Pink, orange and green lines represent experimental data for **1-Y**, **1-Gd**, and **1-Dy**, respectively whereas blue lines constitute calculated TDDFT transitions for **1-Y**.

intense band is located at 250 nm and is primarily composed of a MLCT (metal-to-ligand charge transfer) stemming from the metallocene unit to the ancillary TIP ligand. Remarkably, there are multiple transitions ascribed to π–π* transitions of the ancillary TIP ligand, the strongest of which is in the ultraviolet region positioned at 242 nm. The transition in the visible region (345 nm) is attributed to a ligand-to-metal charge transfer (LMCT) arising from a TIP-based molecular orbital to the d-manifold of the central Y^{III} ion. Similarly, the electronic absorption spectra of **2-RE** were taken in diethyl ether, Fig. S35,† and feature one transition centred at 350 nm. Owing to the similarity between **2-Y** and **2-Dy**, this is tentatively assigned as a LMCT band originating from the DMP ligand.

Ab inito calculations

The isolation of the archetypical tetraiodopyrrole complex **1-RE** and its temperature dependence in RE–I distance prompted the question whether the relaxation behavior of the Dy^{III} ion in **1-Dy** is modulated by Dy–I distance, a feature that could potentially be exploited for temperature-switchable magnetic materials or molecular sensors. To assess the influence of the Dy–I distance on the splitting of the lowest-lying energy spectrum and crystal field parameters, complete active space self-consistent field (CASSCF) calculations were carried out on coordinates obtained from single crystal XRD at 100 K, 200 K and 300 K after optimization of all hydrogen positions. Subsequently, dynamic correlation effects were accounted for *via* N-electron valence perturbation theory (NEVPT2) under consideration of spin–orbit coupling effects *via* a quasi-degenerate (QD) approach. These calculations were carried out using the ORCA 5.0.4 software suite.[55,106]

The low-lying energy spectrum for **1-Dy** was first assessed for the 100 K structure (Fig. 10). The ground state Kramers doublet (KD1) comprises essentially purely of $M_J = |\pm 15/2\rangle$ character, with negligible g_x and g_y contributions rivalling the predominant g_z tensor component. The first excited KD2 is found

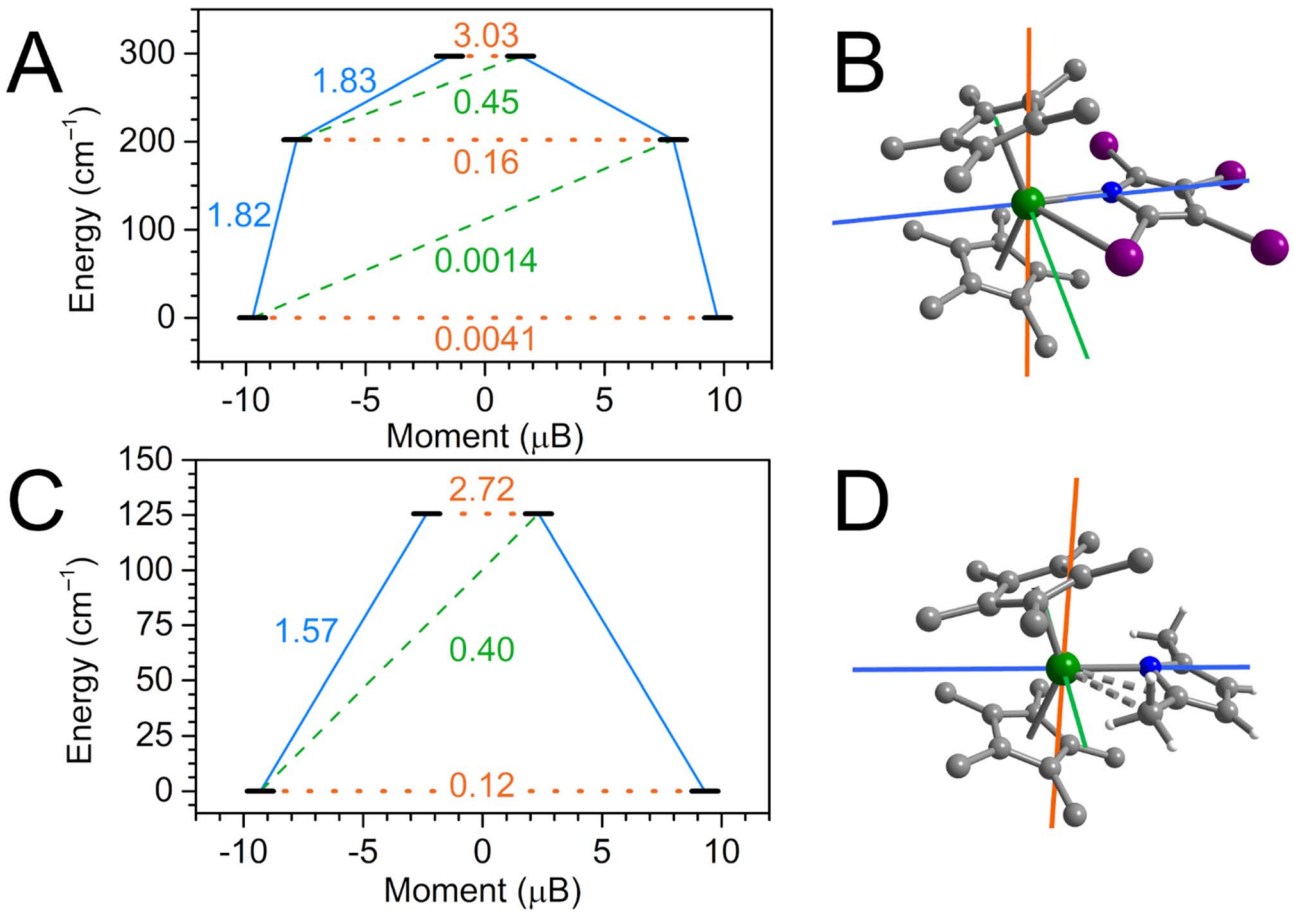

Fig. 10 (A) Estimated relaxation barrier comprising the three lowest-lying Kramers doublets with relaxation pathways shown for Cp*$_2$Dy(TIP) (**1-Dy**). Solid blue and dashed green lines indicate Orbach processes, orange dotted lines indicate quantum tunneling (QTM)/thermally activated QTM pathways. Values next to the arrows correspond to the respective transition magnetic moment (TDM) matrix elements. (B) Plot of the *g*-tensor components calculated for the $|\pm 15/2\rangle$ ground state Kramers doublet of Cp*$_2$Dy(TIP) (**1-Dy**) at 100 K. Color code: g_x (green), g_y (blue) and g_z (orange) with respective compositions 0.0084 (g_x), 0.0161 (g_y) and 19.4562 (g_z). (C) Estimated relaxation barrier comprising the two lowest-lying Kramers doublets with relaxation pathways shown for Cp*$_2$Dy(DMP) (**2-Dy**). (D) Plot of the *g*-tensor components calculated for the $|\pm 15/2\rangle$ ground state Kramers doublet of Cp*$_2$Dy(DMP) (**2-Dy**) at 100 K, with compositions 0.1872 (g_x), 0.5077 (g_y) and 18.5949 (g_z). Green, purple, blue, white, and grey spheres represent Dy, I, N, H, and C atoms, respectively. H atoms of the cyclopentadienyl ligand and co-crystallized dichloromethane are omitted for clarity.

202 cm^{-1} above the ground state, with predominant $M_J = |\pm 13/2\rangle$ composition. However, admixture of the higher lying $|\pm 9/2\rangle$ M_J state results in considerable reduction of the uniaxiality of this state, manifesting in noticeable transversal g_x and g_y contributions (0.3 and 0.7, respectively) to the primary g_z component (15.8). While the transition dipole moment (TDM) connecting ±KD2 is considerably higher than the KD1 TDM it is not large enough to shortcut the barrier. By contrast, the second excited state KD3 at 297 cm^{-1} is no longer ascribable to a singular M_J state due to heavy admixture of excited states, with $g_x = 3.0$ and $g_y = 3.2$ concurring with $g_z = 15.0$. Such strong equatorial fields result in the g_z axis being tilted by 92° in KD2 compared to the ground state g_z orientation, and the TDM crossing the relaxation barrier becoming largest, marking the high end of the estimated relaxation barrier for **1-Dy**.

Having identified the maximum KD determining the magnetic relaxation in **1-Dy**, we then interrogated the effect of increasing Dy–I distances on the M_J composition of KD1–KD3. Surprisingly, it was found that the relative energy of the three lowest-lying KDs remains essentially unchanged between 100 and 300 K, with a maximum change of ∼1% for KD3. The magnetic moment of KD3 decrease continuously upon increasing temperatures, a manifestation of increased excited state admixture. Similarly, the intra KD3 TDM increases slightly by ∼1% from 100–300 K, reaching a maximum TDM at 200 K ∼2% larger than in the ground KD1. Overall, the considerable Dy–I distance modulation observed in single crystal XRD is not reflected in a modulation of the relaxation dynamics in **1-Dy**. Moreover, the calculated crystal field parameters (CFPs) of **1-Dy** vary across the temperatures: Inspecting the dominant CFPs, B_2^0 and B_2^2, together attesting for ∼66% weight of the entire crystal field splitting, B_2^0 decreases from −4.04 (100 K) to −4.14 (300 K) while B_2^2 increases from 6.50 (100 K) to 6.79 (300 K).

The observed marginal changes in the low-lying KD composition and associated relaxation dynamics likely arise from the relatively weak Dy–I interaction compared to the Dy–N distance, which experiences a far less pronounced elongation in comparison and therefore dominates the crystal field (Fig. S66†). In this situation, the Dy–I interactions are far too insignificant to meaningfully modulate the relaxation behaviour in **1-Dy** when the Dy–N distance remains unchanged.

We conducted *ab initio* calculations on **2-Dy** as well. Here, the formal change of α-substituents from iodine to methyl groups serves as an excellent tool to gauge the impact of lighter or heavier atoms within the vicinity of the Dy site on its relaxation behaviour. Similar to **1-Dy**, the ground state KD1 of **2-Dy** is strongly uniaxial with predominant $M_J = |\pm 15/2\rangle$ character, resulting in a $g_z = 18.59$ and small g_x and g_y equatorial contributions. Although small, these equatorial contributions are already 26× and 35× higher for g_x and g_y compared to **1-Dy**, respectively, manifesting in a 28× acceleration of the ground state tunnelling TDM, Fig. 10. Looking at the first excited KD2, lying ∼126 cm^{-1} above KD1, the adversely effect of methyl substitution becomes apparent: the uniaxiality is lost and excited states are strongly admixed, resulting g_x and g_y of 2.39 and 4.68, respectively. It is therefore not surprising that the crossing transition is dominant already in the second excited state, with TDM = 2.72 being 17× higher than in **1-Dy**. This is in excellent qualitative agreement with the experimentally found acceleration in magnetic relaxation from **1-Dy** to **2-Dy**. While their relaxation behaviour has experienced considerable altercations, the crystal fields remain rather comparable: Similar to **1-Dy**, B_2^0 and B_2^2 remain dominant with ∼70% weight, but B_2^2 is larger by 44% to the detriment of B_2^0. A similar study by Mills, Chilton and coworkers on a series of dysprosocenium halobenzene adducts ($Cp^{ttt}Cp^*Dy$)(X-Ph)(Al{$OC(CF_3)$}$_4$) (where X = F, Cl, Br),[107] where the lighter fluorobenzene was found to accelerate magnetic relaxation most whereas heavier bromobenzene showed slowest relaxation.

The *ab initio* calculations showed that the presence of α-methyl substitution compared to iodine dramatically impacts the single ion anisotropy of Dy^{III} in a destructive way. It can be hypothesized that the presence of methyl protons close to the Dy^{III} site in **2-Dy** induces a multitude of low-energy vibrations that facilitate relaxation of the magnetic moment. By contrast, the weak equatorial Dy–I interaction in **1-Dy** barely affects the single ion anisotropy due to the higher atomic weight of iodine *vs.* hydrogen. One can further hypothesize that the coordination of multiple TIP ligands within the equatorial plane, while simultaneously providing strongly electronegative donor ligands in the axial positions could yield a viable route for future stable high-performance SMMs.

Density functional theory

Taking advantage of the diamagnetic nature of the Y^{III} ion, the electronic structure and bonding situation of **1-Y** and **2-Y** were readily deduced through density functional theory. A suitable functional was determined through comparing the computed interatomic distances for six different functions each employing the def2-SVP basis set,[42,49] with those obtained experimentally. For all optimizations, Grimmes' GD3 empirical dispersion correction was included for all atoms,[50,51] as well as a 28 in-core electron pseudopotential for both yttrium and iodine.[45] Of the six functionals examined, the TPSSh functional described best the experimentally-determined structure of **1-Y**. Thus, a final geometry optimization was performed at the def2-TZVP level of theory, again including the GD3 dispersion correction as well as the aforementioned pseudopotentials for both Y and I. A similar procedure was followed to determine the most appropriate description of **2-Y**, Tables S30 and S31.† However, owing to the success of the TPSSh functional in the case of **1-Y**, this functional was also used to allow for comparison of the computational data.

The frontier orbitals of **1-Y** and **2-Y** are depicted in Fig. 11 and S74,† respectively. For both, the highest occupied molecular orbital (HOMO) resides predominantly on the pyrrolyl ligand. However, the lowest unoccupied molecular orbital (LUMO) of **1-Y** is mainly localized on the TIP ligand, whereas it is centred on the metal in **2-Y**. The metal centred LUMO implies that a chemical reduction by one electron will render the highly reducing RE^{II} oxidation state accessible.

Owing to the strongly delocalized structure of **1-Y** and **2-Y**, the bonding interactions were investigated through a natural localized molecular orbital (NLMO)[53] analysis, where the relevant donor/acceptor NLMO interactions are provided in Tables

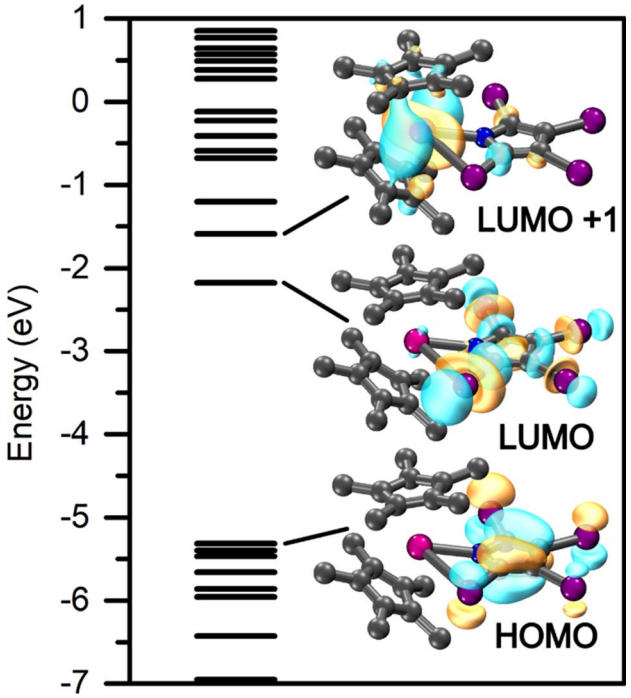

Fig. 11 Calculated frontier orbitals of $Cp^*_2Y(TIP)$, **1-Y**, with the TPSSh functional and def2-TZVP basis set. All isovalues were set to 0.4.

S29 and S32,† respectively. The NLMOs of **1-Y** prove the ionic bonding picture between the Y^{III} cation and the $[TIP]^-$ and $[Cp^*]^-$ anionic ligands. A second-order perturbation analysis of the Y–N interactions are strongly localized toward the coordinating N atom (92.8%), representative of a RE–N bonding situation. The Y–I interaction vastly exceeds that for the chelating nitrogen with summed contributions of 93.16 and 31.42 kcal mol^{-1}, respectively, attributable to the augmented negative charge located on the I-substituents of the TIP ligands. This interaction is also strongly localized (90.6–98.4%) toward the donor I atom. The structure of **1-Y** additionally benefits from small stabilization energies arising from the C–N molecular orbitals (7.58–1.84 kcal mol^{-1}).

The bonding between the yttrium ion and DMP ligand in **2-Y** is most accurately reflected as ionic because the Y–N interactions are similarly polarized toward the N-atom. The strongest interaction arises from the donation of the N lone pair into the d-manifold of the yttrium centre for a summed contribution of impressive 41.12 kcal mol^{-1}, slightly greater than that observed for **1-RE**. A small stabilization energy is detected originating from the C–H bonds of the methyl substituent of the dimethylpyrrolyl ligand (22.09 kcal mol^{-1}). The much lower stabilization energy of **2-Y** relative to that of **1-Y** is allocated to the difference in partial anionic charge on the substituent when comparing iodine to methyl.

Conclusions

Three isostructural mononuclear complexes $Cp^*_2RE(TIP)$ (**1-RE**, RE = Y, Gd and Dy; TIP = 2,3,4,5-tetraiodopyrrolyl) were synthesized through a protonolysis reaction from the respective RE allyl complexes. **1-RE** were characterized through numerous techniques including crystallography, spectroscopy, magnetometry, and computations. Notably, **1-RE** constitute the first compounds installing tetraiodopyrrole as a ligand for any metal. To adequately assess the influence of the I-atom on the electronic properties of the RE metal centre, the analogous 2,5-dimethlpyrrole (DMPH) complex was isolated, $Cp^*_2RE(DMP)$ (**2-RE**, RE = Y, Dy; DMP = 2,5-dimethlpyrrolyl). Owing to the difference in acidity of the DMP analogue relative to other pyrrole derivatives, an alternative synthetic route was necessary highlighting the limits of the protonolysis reaction pathway involving $Cp^*_2RE(\eta^3\text{-}C_3H_5)$. Here, the DMP ligand coordinates in a similar fashion to the TIP ligand rendering it an appropriate comparison. The introduction of the TIP ligand to coordination chemistry represents a promising route to introduce intermolecular halogen bonding interactions between molecules within a crystal lattice. The study of such halogen bonding interactions poses a critical development in the field of quantum information science as these interactions can help prevent pivotal rotations and vibrations which are thought to be responsible for fast magnetic relaxation pathways. The Dy analogue, **1-Dy**, is a zero-field single-molecule magnet, where *ab initio* calculations uncovered the influence of the Dy–I interatomic distance on the electronic structure of the Dy^{III} ion. In comparison, the methyl-substituted complex, **2-Dy** exhibits faster magnetic relaxation likely stemming from a combination of decreased donor capacity of the TIP anion relative to DMP and the mitigation of low energy vibrations residing close to the metal centre.

In both cases, DFT calculations uncover the bonding situations of both **1-Y**, and **2-Y** respectively. The introduction of ligand scaffolds bearing covalently bonded I-atoms represent an exciting frontier of research where the intermolecular interactions of these species can potentially mitigate fast, vibrationally activated, relaxation pathways. From a more general perspective, the introduction of tetraiodopyrrole into coordination chemistry may inspire the pursuit of coordination compounds with the entirety of the transition metals that could be relevant for catalysis and small molecule activation.

Data availability

All computational data, spectroscopic data, supplementary figures and tables, and detailed crystallographic information can be found in the ESI.† Crystallographic data are available *via* the Cambridge Crystallographic Data Centre (CCDC): 2350192–2350216. The data supporting this article have been included as part of the ESI.†

Author contributions

F. D. prepared and characterised all compounds. S. J. provided experimental assistance. F. B. performed *ab initio* calculations. S. M. G. collected and interpreted EPR data. S. D. assisted with data analysis, formulated, and directed the research, and wrote the manuscript with input from all authors.

Conflicts of interest

There are no conflicts to declare.

Acknowledgements

This work was funded in part through the National Science Foundation (NSF) Faculty Early Career Development Program (CAREER) CHE-2339595. S.D. is grateful to the Department of Chemistry at Michigan State University (MSU) for generous start-up funds. We are grateful to Dr Rui Huang and Dr Richard Staples (MSU) for assistance with CHN and X-ray diffraction analyses respectively. We thank Ernesto Castellanos for experimental assistance. This work was supported in part through computational resources and services provided by the Institute for Cyber-Enabled Research at MSU. The LANL EPR Lab is supported by the U.S. Department of Energy, Office of Science, Office of Basic Energy Sciences, Heavy Element Chemistry Program (2020LANLE372) and the Laboratory Directed Research and Development program at LANL (20230399ER). LANL is managed by Triad National Security, LLC, for the NNSA of the U.S. Department of Energy (contract 89233218CNA000001).

Notes and references

1 J. C. Vanjak, B. O. Wilkins, V. Vieru, N. S. Bhuvanesh, J. H. Reibenspies, C. D. Martin, L. F. Chibotaru and M. Nippe, *J. Am. Chem. Soc.*, 2022, **144**, 17743–17747.
2 A. H. Vincent, Y. L. Whyatt, N. F. Chilton and J. R. Long, *J. Am. Chem. Soc.*, 2023, **145**, 1572–1579.
3 X. Sun, L. Münzfeld, D. Jin, A. Hauser and P. W. Roesky, *Chem. Commun.*, 2022, **58**, 7976–7979.
4 J. Liu, K. Singh, S. Dutta, Z. Feng, D. Koley, G. Tan and X. Wang, *Dalton Trans.*, 2021, **50**, 5552–5556.
5 L. Münzfeld, X. Sun, S. Schlittenhardt, C. Schoo, A. Hauser, S. Gillhuber, F. Weigend, M. Ruben and P. W. Roesky, *Chem. Sci.*, 2022, **13**, 945–954.
6 F. Jaroschik, T. Shima, X. Li, K. Mori, L. Ricard, X.-F. Le Goff, F. Nief and Z. Hou, *Organometallics*, 2007, **26**, 5654–5660.
7 S.-M. Chen, J. Xiong, Y.-Q. Zhang, Q. Yuan, B.-W. Wang and S. Gao, *Chem. Sci.*, 2018, **9**, 7540–7545.
8 P. Evans, D. Reta, G. F. S. Whitehead, N. F. Chilton and D. P. Mills, *J. Am. Chem. Soc.*, 2019, **141**, 19935–19940.
9 F.-S. Guo, M. He, G.-Z. Huang, S. R. Giblin, D. Billington, F. W. Heinemann, M.-L. Tong, A. Mansikkamäki and R. A. Layfield, *Inorg. Chem.*, 2022, **61**, 6017–6025.
10 F. Nief, D. Turcitu and L. Ricard, *Chem. Commun.*, 2002, 1646–1647.
11 E. R. Pugliese, F. Benner and S. Demir, *Chem.–Eur. J.*, 2023, **29**, e202302687.
12 L. Knorr, *Ber. Dtsch. Chem. Ges.*, 1884, **17**, 2863–2870.
13 C. Paal, *Ber. Dtsch. Chem. Ges.*, 1884, **17**, 2756–2767.
14 T. W. Lyons and M. S. Sanford, *Chem. Rev.*, 2010, **110**, 1147–1169.
15 P.-B. Jin, K.-X. Yu, Q.-C. Luo, Y.-Y. Liu, Y.-Q. Zhai and Y.-Z. Zheng, *Angew. Chem., Int. Ed.*, 2022, **61**, e202203285.
16 P.-B. Jin, Q.-C. Luo, Y.-Q. Zhai, Y.-D. Wang, Y. Ma, L. Tian, X. Zhang, C. Ke, X.-F. Zhang, Y. Lv and Y.-Z. Zheng, *iScience*, 2021, **24**, 102760.
17 P.-B. Jin, Y.-Q. Zhai, K.-X. Yu, R. E. P. Winpenny and Y.-Z. Zheng, *Angew. Chem., Int. Ed.*, 2020, **59**, 9350–9354.
18 J.-M. Lehn, *Angew Chem. Int. Ed. Engl.*, 1988, **27**, 89–112.
19 P. J. Costa, *Phys. Sci. Rev.*, 2017, **2**, 20170136.
20 T. Clark, M. Hennemann, J. S. Murray and P. Politzer, *J. Mol. Model.*, 2007, **13**, 291–296.
21 L. C. Gilday, S. W. Robinson, T. A. Barendt, M. J. Langton, B. R. Mullaney and P. D. Beer, *Chem. Rev.*, 2015, **115**, 7118–7195.
22 H. Bock and S. Holl, *Z. Naturforsch., B: J. Chem. Sci.*, 2002, **57**, 843–858.
23 M. A. Bondarenko, A. S. Novikov, P. A. Abramov, I. F. Sakhapov, M. N. Sokolov and S. A. Adonin, *J. Mol. Struct.*, 2021, **1230**, 129931–129936.
24 P. M. J. Szell, S. Zablotny and D. L. Bryce, *Nat. Commun.*, 2019, **10**, 916–924.
25 G. L. Ciamician and M. Dennstedt, *Ber. Dtsch. Chem. Ges.*, 1882, **15**, 2579–2585.
26 J. Chang, G. Zhao, X. Zhao, C. He, S. Pang and J. M. Shreeve, *Acc. Chem. Res.*, 2021, **54**, 332–343.
27 G. Mínguez Espallargas, L. Brammer, D. R. Allan, C. R. Pulham, N. Robertson and J. E. Warren, *J. Am. Chem. Soc.*, 2008, **130**, 9058–9071.
28 A. Forni, P. Metrangolo, T. Pilati and G. Resnati, *Cryst. Growth Des.*, 2004, **4**, 291–295.
29 W. J. Evans, S. A. Kozimor, J. W. Ziller and N. Kaltsoyannis, *J. Am. Chem. Soc.*, 2004, **126**, 14533–14547.
30 L. C. H. Gerber, R. R. Schrock and P. Müller, *Organometallics*, 2013, **32**, 2373–2378.
31 S. Demir, J. M. Zadrozny, M. Nippe and J. R. Long, *J. Am. Chem. Soc.*, 2012, **134**, 18546–18549.
32 W. J. Evans, S. A. Kozimor, J. C. Brady, B. L. Davis, G. W. Nyce, C. A. Seibel, J. W. Ziller and R. J. Doedens, *Organometallics*, 2005, **24**, 2269–2278.
33 *CrysAlisPro Software System*, Rigaku Corporation, Oxford2020.
34 *SCALE3 ABSPACK Empirical Absorption Correction, CrysAlis Pro - Software Package*, Rigaku Corporation, Oxford2020.
35 G. Sheldrick, *Acta Crystallogr., Sect. A: Found. Crystallogr.*, 2015, **71**, 3–8.
36 G. Sheldrick, *Acta Crystallogr., Sect. C: Struct. Chem.*, 2015, **71**, 3–8.
37 O. V. Dolomanov, L. J. Bourhis, R. J. Gildea, J. A. K. Howard and H. Puschmann, *J. Appl. Crystallogr.*, 2009, **42**, 339–341.
38 H. Bock, S. Holl and V. Krenzel, *Z. Naturforsch., B: J. Chem. Sci.*, 2001, **56**, 13–24.
39 G. A. Bain and J. F. Berry, *J. Chem. Educ.*, 2008, **85**, 532.
40 S. Stoll and A. Schweiger, *J. Magn. Reson.*, 2006, **178**, 42–55.
41 J. R. Pliego, *Chem. Phys. Lett.*, 2003, **367**, 145–149.
42 F. Weigend and R. Ahlrichs, *Phys. Chem. Chem. Phys.*, 2005, **7**, 3297–3305.

43 B. P. Pritchard, D. Altarawy, B. Didier, T. D. Gibson and T. L. Windus, *J. Chem. Inf. Model.*, 2019, **59**, 4814–4820.
44 T. Yanai, D. P. Tew and N. C. Handy, *Chem. Phys. Lett.*, 2004, **393**, 51–57.
45 K. A. Peterson, D. Figgen, M. Dolg and H. Stoll, *J. Chem. Phys.*, 2007, **126**, 124101.
46 V. Barone and M. Cossi, *J. Phys. Chem. A*, 1998, **102**, 1995–2001.
47 M. Cossi, N. Rega, G. Scalmani and V. Barone, *J. Comput. Chem.*, 2003, **24**, 669–681.
48 M. J. Frisch, G. W. Trucks, H. B. Schlegel, G. E. Scuseria, M. A. Robb, J. R. Cheeseman, G. Scalmani, V. Barone, G. A. Petersson, H. Nakatsuji, X. Li, M. Caricato, A. V. Marenich, J. Bloino, B. G. Janesko, R. Gomperts, B. Mennucci, H. P. Hratchian, J. V. Ortiz, A. F. Izmaylov, J. L. Sonnenberg, D. Williams-Young, F. Ding, F. Lipparini, F. Egidi, J. Goings, B. Peng, A. Petrone, T. Henderson, D. Ranasinghe, V. G. Zakrzewski, J. Gao, N. Rega, G. Zheng, W. Liang, M. Hada, M. Ehara, K. Toyota, R. Fukuda, J. Hasegawa, M. Ishida, T. Nakajima, Y. Honda, O. Kitao, H. Nakai, T. Vreven, K. Throssell, J. A. Montgomery Jr, J. E. Peralta, F. Ogliaro, M. J. Bearpark, J. J. Heyd, E. N. Brothers, K. N. Kudin, V. N. Staroverov, T. A. Keith, R. Kobayashi, J. Normand, K. Raghavachari, A. P. Rendell, J. C. Burant, S. S. Iyengar, J. Tomasi, M. Cossi, J. M. Millam, M. Klene, C. Adamo, R. Cammi, J. W. Ochterski, R. L. Martin, K. Morokuma, O. Farkas, J. B. Foresman and D. J. Fox, *Gaussian 16, Rev. B01*, Gaussian, Inc., Wallingford CT, 2016.
49 D. Andrae, U. Häußermann, M. Dolg, H. Stoll and H. Preuß, *Theor. Chim. Acta*, 1990, **77**, 123–141.
50 S. Grimme, J. Antony, S. Ehrlich and H. Krieg, *J. Chem. Phys.*, 2010, **132**, 154104.
51 D. G. A. Smith, L. A. Burns, K. Patkowski and C. D. Sherrill, *J. Phys. Chem. Lett.*, 2016, **7**, 2197–2203.
52 L. Münzfeld, C. Schoo, S. Bestgen, E. Moreno-Pineda, R. Köppe, M. Ruben and P. W. Roesky, *Nat. Commun.*, 2019, **10**, 3135.
53 A. E. Reed and F. Weinhold, *J. Chem. Phys.*, 1985, **83**, 1736–1740.
54 F. Neese, *Wiley Interdiscip. Rev.: Comput. Mol. Sci.*, 2012, **2**, 73–78.
55 F. Neese, *Wiley Interdiscip. Rev.: Comput. Mol. Sci.*, 2022, **12**, e1606.
56 P. M. Zeimentz, S. Arndt, B. R. Elvidge and J. Okuda, *Chem. Rev.*, 2006, **106**, 2404–2433.
57 B. M. Day, F.-S. Guo and R. A. Layfield, *Acc. Chem. Res.*, 2018, **51**, 1880–1889.
58 M. T. Dumas, T. F. Jenkins, J. C. Wedal, J. W. Ziller, F. Furche and W. J. Evans, *Organometallics*, 2021, **40**, 735–741.
59 F. Delano IV, F. Benner, S. Jang and S. Demir, *Inorg. Chem.*, 2023, **62**, 14604–14614.
60 S.-S. Liu, S. Gao, J. W. Ziller and W. J. Evans, *Dalton Trans.*, 2014, **43**, 15526–15531.
61 M. E. Fieser, T. J. Mueller, J. E. Bates, J. W. Ziller, F. Furche and W. J. Evans, *Organometallics*, 2014, **33**, 3882–3890.
62 M. Rupp, R. Korner and I. V. Tetko, *Comb. Chem. High Throughput Screening*, 2011, **14**, 307–327.
63 F. Delano IV, E. Castellanos, J. McCracken and S. Demir, *Chem. Sci.*, 2021, **12**, 15219–15228.
64 C. A. Gould, E. Mu, V. Vieru, L. E. Darago, K. Chakarawet, M. I. Gonzalez, S. Demir and J. R. Long, *J. Am. Chem. Soc.*, 2020, **142**, 21197–21209.
65 F. Benner and S. Demir, *Inorg. Chem. Front.*, 2023, **10**, 4981–4992.
66 F. Benner, L. L. Droitte, O. Cador, B. L. Guennic and S. Demir, *Chem. Sci.*, 2023, **14**, 5577–5592.
67 M. R. MacDonald, J. W. Ziller and W. J. Evans, *Inorg. Chem.*, 2011, **50**, 4092–4106.
68 C. A. Gould, L. E. Darago, M. I. Gonzalez, S. Demir and J. R. Long, *Angew. Chem., Int. Ed.*, 2017, **56**, 10103–10107.
69 E. R. Pugliese, F. Benner, E. Castellanos, F. Delano IV and S. Demir, *Inorg. Chem.*, 2022, **61**, 2444–2454.
70 F. Delano IV and S. Demir, *Cryst. Growth Des.*, 2023, **23**, 3134–3143.
71 F. Delano IV, S. Deshapriya and S. Demir, *Inorg. Chem.*, 2024, **63**, 9659–9669.
72 P.-B. Jin, Q.-C. Luo, G. K. Gransbury, I. J. Vitorica-Yrezabal, T. Hajdu, I. Strashnov, E. J. L. McInnes, R. E. P. Winpenny, N. F. Chilton, D. P. Mills and Y.-Z. Zheng, *J. Am. Chem. Soc.*, 2023, **145**, 27993–28009.
73 Y. Wang, Q.-C. Luo, Y.-Q. Zhai, P.-B. Jin, Z. Fu, Q. Sun, F.-N. Li and Y.-Z. Zheng, *Cryst. Growth Des.*, 2022, **22**, 6398–6404.
74 P.-B. Jin, K.-X. Yu, Y.-Q. Zhai, Q.-C. Luo, Y.-D. Wang, X.-F. Zhang, Y. Lv and Y.-Z. Zheng, *Chin. J. Chem.*, 2021, **39**, 1635–1640.
75 F. Delano, S. Deshapriya and S. Demir, *Polyhedron*, 2024, **249**, 116785.
76 Y. Luo and J. Chen, *J. Organomet. Chem.*, 2018, **863**, 10–14.
77 R. D. Shannon, *Acta Crystallogr., Sect. A: Cryst. Phys., Diffr., Theor. Gen. Crystallogr.*, 1976, **32**, 751–767.
78 K. L. M. Harriman, J. L. Brosmer, L. Ungur, P. L. Diaconescu and M. Murugesu, *J. Am. Chem. Soc.*, 2017, **139**, 1420–1423.
79 Y.-S. Meng, Y.-Q. Zhang, Z.-M. Wang, B.-W. Wang and S. Gao, *Chem.–Eur. J.*, 2016, **22**, 12724–12731.
80 M. Li, H. Wu, Z. Xia, L. Ungur, D. Liu, L. F. Chibotaru, H. Ke, S. Chen and S. Gao, *Inorg. Chem.*, 2020, **59**, 7158–7166.
81 M. Mantina, A. C. Chamberlin, R. Valero, C. J. Cramer and D. G. Truhlar, *J. Phys. Chem. A*, 2009, **113**, 5806–5812.
82 A. Mukherjee, S. Tothadi and G. R. Desiraju, *Acc. Chem. Res.*, 2014, **47**, 2514–2524.
83 J. S. Murray, M. C. Concha, P. Lane, P. Hobza and P. Politzer, *J. Mol. Model.*, 2008, **14**, 699–704.
84 W. Wang, N.-B. Wong, W. Zheng and A. Tian, *J. Phys. Chem. A*, 2004, **108**, 1799–1805.
85 P. Politzer, J. S. Murray and T. Clark, *Phys. Chem. Chem. Phys.*, 2013, **15**, 11178–11189.
86 M. P. Mitoraj and A. Michalak, *J. Mol. Model.*, 2013, **19**, 4681–4688.
87 S. V. Rosokha, C. L. Stern and J. T. Ritzert, *Chem.–Eur. J.*, 2013, **19**, 8774–8788.

88 M. R. Saber and K. R. Dunbar, *Chem. Commun.*, 2014, **50**, 12266–12269.
89 H. L. C. Feltham and S. Brooker, *Coord. Chem. Rev.*, 2014, **276**, 1–33.
90 O. Kahn, *Molecular Magnetism*, VCH, 1993.
91 N. F. Chilton, *Inorg. Chem.*, 2015, **54**, 2097–2099.
92 C. A. Gould, K. R. McClain, D. Reta, J. G. C. Kragskow, D. A. Marchiori, E. Lachman, E.-S. Choi, J. G. Analytis, R. D. Britt, N. F. Chilton, B. G. Harvey and J. R. Long, *Science*, 2022, **375**, 198–202.
93 S. Kumar Kushvaha, P. Ravichandran, C. Dan, L. Ungur, N. Suryadevara, M. Ruben and K. Chandra Mondal, *Eur. J. Inorg. Chem.*, 2024, **27**, e202300598.
94 P. Zhang, F. Benner, N. F. Chilton and S. Demir, *Chem*, 2022, **8**, 717–730.
95 P. Zhang, R. Nabi, J. K. Staab, N. F. Chilton and S. Demir, *J. Am. Chem. Soc.*, 2023, **145**, 9152–9163.
96 L. Devkota, D. J. SantaLucia, A. M. Wheaton, A. J. Pienkos, S. V. Lindeman, J. Krzystek, M. Ozerov, J. F. Berry, J. Telser and A. T. Fiedler, *Inorg. Chem.*, 2023, **62**, 5984–6002.
97 T. A. Betley and J. C. Peters, *Inorg. Chem.*, 2003, **42**, 5074–5084.
98 P. Pyykkö, *Annu. Rev. Phys. Chem.*, 2012, **63**, 45–64.
99 S. Demir, J. M. Zadrozny and J. R. Long, *Chem.–Eur. J.*, 2014, **20**, 9524–9529.
100 S. Demir, M. D. Boshart, J. F. Corbey, D. H. Woen, M. I. Gonzalez, J. W. Ziller, K. R. Meihaus, J. R. Long and W. J. Evans, *Inorg. Chem.*, 2017, **56**, 15049–15056.
101 D. Reta and N. F. Chilton, *Phys. Chem. Chem. Phys.*, 2019, **21**, 23567–23575.
102 P. Zhang, M. Perfetti, M. Kern, P. P. Hallmen, L. Ungur, S. Lenz, M. R. Ringenberg, W. Frey, H. Stoll, G. Rauhut and J. van Slageren, *Chem. Sci.*, 2018, **9**, 1221–1230.
103 T. P. Gompa, S. M. Greer, N. T. Rice, N. Jiang, J. Telser, A. Ozarowski, B. W. Stein and H. S. La Pierre, *Inorg. Chem.*, 2021, **60**, 9064–9073.
104 J. Telser, in *eMagRes*, John Wiley & Sons, Ltd, 2017, pp. 207–234.
105 C. A. P. Goodwin, D. Reta, F. Ortu, N. F. Chilton and D. P. Mills, *J. Am. Chem. Soc.*, 2017, **139**, 18714–18724.
106 Y. Guo, K. Sivalingam, C. Kollmar and F. Neese, *J. Chem. Phys.*, 2021, **154**, 214113.
107 S. C. Corner, G. K. Gransbury, I. J. Vitorica-Yrezabal, G. F. S. Whitehead, N. F. Chilton and D. P. Mills, *Inorg. Chem.*, 2024, **63**, 9552–9561.